A critical period of translational control during brain development at codon resolution

Dermot Harnett,[1,9,*] Mateusz C. Ambrozkiewicz,[2,9,*] Ulrike Zinnall,[1] Alexandra Rusanova,[3] Ekaterina Borisova,[3] Rike Dannenberg,[2] Koshi Imami,[4,5] Agnieszka Münster-Wandowski,[6] Beatrix Fauler,[7] Thorsten Mielke,[7] Matthias Selbach,[5] Markus Landthaler,[1] Christian M.T. Spahn,[8] Victor Tarabykin,[2,3,†] Uwe Ohler,[1,†] Matthew L. Kraushar[7,†,*]

[1] Berlin Institute for Medical Systems Biology, Max Delbrück Center for Molecular Medicine, 10115 Berlin, Germany

[2] Institute of Cell Biology and Neurobiology, Charité-Universitätsmedizin Berlin, corporate member of Freie Universität Berlin, Humboldt-Universität zu Berlin, and Berlin Institute of Health, 10117 Berlin, Germany

[3] Institute of Neuroscience, Lobachevsky University of Nizhny Novgorod, pr. Gagarina 24, Nizhny Novgorod, Russian Federation

[4] Department of Molecular and Cellular BioAnalysis, Graduate School of Pharmaceutical Sciences, Kyoto University, Kyoto 606-8501, Japan

[5] Max Delbrück Center for Molecular Medicine, 13092 Berlin, Germany

[6] Institute of Neuroanatomy, Charité-Universitätsmedizin Berlin, 10117 Berlin, Germany

[7] Max Planck Institute for Molecular Genetics, 14195 Berlin, Germany

[8] Institute of Medical Physics and Biophysics, Charité-Universitätsmedizin Berlin, 10117 Berlin, Germany

[9] These authors contributed equally

[†] Senior author

*Correspondence:
dermot.harnett@mdc-berlin.de (D.H.);
mateusz-cyryl.ambrozkiewicz@charite.de (M.C.A.);
matthew.kraushar@molgen.mpg.de (M.L.K.)

Abstract

Translation modulates the timing and amplification of gene expression after transcription. Brain development requires uniquely complex gene expression patterns, but large-scale measurements of translation directly in the prenatal brain are lacking. We measure the reactants, synthesis, and products of translation spanning mouse neocortex neurogenesis, and discover a transient window of dynamic regulation at mid-gestation. Timed translation upregulation of chromatin binding proteins like Satb2, which is essential for neuronal subtype differentiation, restricts protein expression in neuronal lineages despite broad transcriptional priming in progenitors. In contrast, translation downregulation of ribosomal proteins sharply decreases ribosome number, coinciding with a major shift in protein synthesis dynamics at mid-gestation. Changing levels of eIF4EBP1, a direct inhibitor of ribosomal protein translation, are concurrent with ribosome downregulation and controls Satb2 fate acquisition during neuronal differentiation. Thus, the refinement of transcriptional programs by translation is central to the molecular logic of brain development. Modeling of the developmental neocortex translatome is provided as an open-source searchable resource: https://shiny.mdc-berlin.de/cortexomics/.

Introduction

Changes in translation activity can lead to significant discrepancies between mRNA and protein for the same gene, and are a hallmark of many dynamic cellular transition states [1]. Dynamic cellular transitions are uniquely complex during brain development from neural stem cells, which must deploy highly sophisticated gene expression programs [2,3]. In evolutionarily advanced brain regions like the neocortex, a cell's transcriptional signature alone appears insufficient to account for the enormous cellular diversity, with recent single-cell RNA sequencing (scRNA-seq) analyses supporting this idea [4–7]. While transcriptional profiles define broad classes of neurons and non-neuronal cells, a striking conclusion from these studies was the degree of homogeneity in mRNA pools across neuronal lineages during stem cell differentiation [4], and between distinct neuronal circuits postnatally [7]. Considering whether neuronal differentiation in the neocortex utilizes a more "generic" transcriptome [4] has led the field to ask recently whether neuronal identity is a stochastic rather than deterministic process [8]. Do "progenitors play dice" [9] while deciding their neuronal fate? Thus, the blueprint of gene expression in evolutionarily advanced brain regions is likely a multilayered, progressive

refinement – including and beyond transcription [3]. Neocortex development may thus represent a particularly dynamic cellular system of translational control [10,11].

Direct measurements of protein synthesis would provide a clearer picture of functional gene expression in the developing brain; however, a large-scale high-resolution analysis of mRNA translation during neurogenesis has lagged behind transcriptome analysis, in part due to current technical limitations in protein measurement. Recent work suggests that targeted and selective protein synthesis refines the output of gene expression in brain development [5,12–16]. Importantly, abnormal ribosome levels and disrupted translation was found recently to be a mid-gestation etiology of neurodevelopmental disorders [17]. However, how ribosomes decode mRNA in the transcriptome-to-proteome transition during developmental neurogenesis remains unknown.

To circumvent these challenges and measure the temporal dynamics of the reactants, synthesis, and products of mRNA translation during brain development, we performed sequencing of ribosome-protected mRNA fragments (Ribo-seq; ribosome profiling) [18] in parallel with RNA-seq, tRNA qPCR array, and mass spectrometry across five stages of mouse neocortex neurogenesis. By capturing ribosome-mRNA interactions at codon-level resolution, we find that ~ 18 % of mRNAs change translation efficiency in the progressive specification of neural stem cells to post-mitotic neurons, with a transient peak window of dynamic translation at mid-gestation.

Divergent cellular pathways are impacted by translation upregulation vs. downregulation during neurogenesis. Chromatin binding proteins like *Satb2*, essential for the differentiation of neuronal subtypes [19], are the most translationally upregulated mRNAs. We find *Satb2* mRNA is transcribed unexpectedly broadly in neuronal lineages, but achieves restricted neuronal subtype-specific protein expression by timed translation. In contrast, ribosomal proteins are the most translationally downregulated, coinciding with dynamic expression of eIF4EBP1, a translational repressor targeting these transcripts directly [20,21]. An acute decrease in ribosome number coincides with widespread changes in global translation kinetics at mid-gestation – a critical period for neurodevelopmental pathology [17]. Finally, *in utero* knockdown of eIF4EBP1 in neural progenitors to disrupt the balance of translation during this window leads to decreased specification of the Satb2 neuronal lineage and migration arrest.

Thus, by mapping the quantitative landscape of the transcriptome-to-proteome transition in the neocortex, we find that protein synthesis is a powerful and widespread layer of gene expression regulation that shifts kinetics and impacts neuronal specification during development. We provide the developmental neocortex translatome as an open-source searchable web resource: https://shiny.mdc-berlin.de/cortexomics/.

Results

Deep sequencing of translation reveals a spike in regulation during neurodevelopment

We focused our study on the mammalian neocortex, an evolutionarily advanced and dynamic developmental system with a tightly timed sequence of neurogenesis [2,22] (**Fig. 1a**). At embryonic day 12.5 (E12.5) this predominantly stem cell tissue gives birth to its first neurons. Neurons born early at E12.5 form distinct connections and control different functions than those born later at E15.5. By postnatal day 0 (P0), neurogenesis is largely complete. The timed sequence of gene expression is essential to specify neuronal fate from the stem cell pool.

We designed a strategy to analyze the major reactants, synthesis, and products of mRNA translation across five stages encompassing neocortex neurogenesis (**Fig. 1a**), including Ribo-seq measurement of ribosome-mRNA interactions, in parallel with RNA-seq, tRNA qPCR array, and mass spectrometry. Ribo-seq measures 80S ribosomes bound to the open reading frame of mRNA – a quantitative indicator of active protein synthesis at codon-level resolution [18]. Optimizations for analysis of neocortex ribosomes *ex vivo* circumvented the requirement for pharmacological ribosome stalling with cycloheximide [15], which introduces ribosome footprint redistribution artifacts [23], and enabled efficient nuclease digestion to generate high fidelity ribosome-protected mRNA fragments (RPFs) (**Extended Data Fig. 1**). We obtained mRNA transcripts per-million (TPM) and RPF densities for 22,373 genes (**Extended Data Fig. 2a, Supplementary Table 1**). Reproducibility of both mRNA and RPF measurements permitted reliable calculation of mRNA translation efficiency (**Extended Data Fig. 2b-e**), which represents the ratio between ribosome binding to an mRNA's coding sequence and the mRNA's level overall (**Fig. 1b**). As a quality control, we focused further analysis on coding sequences with 32 or more Ribo-seq footprints in at least one stage as per [24], which resulted in a set of 12,228 translated GENCODE-annotated transcripts.

To detect translation-specific gene expression regulation, we first calculated fold changes between sequential time points in mRNA or RPF vs. protein (**Fig. 1c, Supplementary Table 2**). While gene expression overall is quite stable between E12.5 and E14, a burst of regulation occurs at E15.5 at both transcriptional and translational levels, with a significant impact on the proteome. However, robust RPF fold changes persist until P0, with mRNA changes less pronounced. Calculation of translation efficiency highlighted a transient window of robust regulation at E15.5, coinciding with the major transition in neuronal fate specification. Translation efficiency upregulation was found to occur in 1,129 genes and downregulation in 1,131 genes. A further 2,253 genes change in steady state mRNA only, without any significant translation efficiency change. Thus, we estimate ~ 18 % of the transcriptome is dynamically translated across neocortex neurogenesis, with an acute inflection point during the mid-neurogenesis transition at E15.5.

Our Ribo-seq data shows a higher correlation with protein level changes than RNA-seq data, (**Fig. 1c**). We decomposed technical and systematic variation in protein levels, and estimated proportions explained by RNA-seq vs. Ribo-seq [25] (**Fig. 1d and Extended Data Fig. 2f**). A majority of protein level variance is accounted for by RNAseq, in agreement with prior observations [25,26]. However, Ribo-seq consistently explains a higher fraction of protein variation than RNA-seq at each developmental stage, especially for proteins with increasing levels – concordant with Ribo-seq being a direct measure of protein synthesis. The protein level predictivity of Ribo-seq was particularly pronounced for genes with changing translation efficiency.

Thus, our data enable detection of regulation that impacts the protein output of gene expression, which includes a transient window of robust translation control at E15.5.

Translation upregulation of chromatin binding proteins like Satb2 establishes neuronal fate

We first focused on the cohort of genes that are translation efficiency upregulated across neurogenesis after E12.5, to identify essential neurodevelopmental proteins with dynamic translation. Gene ontology analysis demonstrated chromatin binding proteins are particularly subject to translation upregulation (**Fig. 2a**). Chromatin binding proteins like transcription factors have a powerful influence on the neuronal fate of stem cells, which is tightly

132 coordinated in developmental time. *Early*-born post-mitotic neurons ultimately express
133 transcription factors like Bcl11b, which drives them to connect *sub*-cortically [27]. In contrast,
134 *late*-born post-mitotic neurons after E15.5 ultimately express transcription factors like Satb2,
135 which drives them to connect *intra*-cortically [19,28]. How proteins like transcription factors
136 achieve neuronal subtype and temporally restricted expression is a critical unresolved question.
137

138 Among the most translationally upregulated neurodevelopmental proteins discovered in our
139 data is the essential, late-born upper layer neuron transcription factor Satb2 (**Fig. 2b**). We
140 assessed the trajectory of Satb2 synthesis in our RNA-seq, Ribo-seq, and mass spec data
141 along with calculated translation efficiency; in comparison to the intermediate filament protein
142 Nes expressed by neural stem cells [29], and early-stage transcription factor Bcl11b expressed
143 in neurons positioned adjacent to the later Satb2 lineage. As expected, Nes demonstrates
144 predominantly transcriptionally driven expression downregulation, as the neural stem cell pool
145 is depleted by neuronal differentiation [30]. Bcl11b is expressed in the early-born lineage with
146 high concordance between RNA-seq and Ribo-seq, and with low fluctuations in translation
147 efficiency. In contrast, fold changes in Satb2 Ribo-seq and MS signal are in excess of the
148 RNA-seq, with 2-fold translation efficiency upregulation reaching a plateau at E15.5. These
149 data suggest that *Satb2* expression is amplified by translation.
150

151 To begin testing the hypothesis that *Satb2* mRNA undergoes translation regulation, we first
152 examined the cellular distribution of *Satb2* mRNA in scRNA-seq neuronal lineage-tracing data
153 [4]. Surprisingly, we found that *Satb2* mRNA is robustly expressed in differentiated neurons of
154 both the early- *and* late-born lineages (**Fig. 2c**) – an apparent discrepancy with previous
155 findings for Satb2 protein [19,28]. Thus, transcription of this upper layer program may occur in
156 neuronal lineages that include lower layers, and outside of the expected protein distribution.
157

158 To directly visualize the spatiotemporal expression of *Satb2* mRNA and protein, we performed
159 fluorescence *in situ* hybridization and immunohistochemistry in neocortical coronal sections
160 (**Fig. 2d**), with probe and antibody specificity confirmed in *Satb2*$^{-/-}$ brains (**Extended**
161 **Data Fig. 3a**), and signal quantified per cell (**Fig. 2e and Extended Data Fig. 3b,**
162 **Supplementary Table 3**). At the onset of neurogenesis E12.5, initial scattered, weak Bcl11b
163 protein signal is congruent with its mRNA signal in post-mitotic neurons. Satb2 protein is
164 undetectable; however, we observed robust *Satb2* mRNA signal throughout the neocortex,

from the ventricular zone in multipotent progenitors and throughout the nascent cortical plate in early-born post-mitotic neurons. In neurons differentiating in the cortical plate, almost half of all *Satb2* mRNA clusters colocalize with *Bcl11b* mRNA, which rarely occurs in the stem cell niche of the ventricular zone.

Weak Satb2 protein expression is first detected at E14.5, in contrast to strong Bcl11b protein now appearing in post-mitotic neurons. Only by E16.5 is Satb2 protein expression robust. Satb2 mRNA and protein are broadly expressed across upper layers, lower layers, and the intermediate zone by E16.5. However, neurons having migrated to their ultimate position in upper layers almost exclusively express Satb2 rather than Bcl11b protein, in contrast to regions like the intermediate zone where neurons continue to migrate.

Taken together, *Satb2* mRNA and protein expression are divergent in developmental time and space. This divergence includes broad, early *Satb2* mRNA expression in multipotent progenitors despite Satb2 protein ultimately restricted to upper layer post-mitotic neurons later in development. Furthermore, while the distribution and colocalization of mRNA for *Bcl11b* and *Satb2* neuronal programs remains broad and overlapping in post-mitotic neurons at E16.5, corresponding protein expression is more exclusive, with the intermediate zone a transitory region where specification at both the mRNA and protein levels are still lacking distinction. Thus, our bioinformatics analysis identifies *Satb2* as a translationally upregulated mRNA, for which we observe incongruent spatiotemporal mRNA-protein expression *in situ*.

Translation establishes the balance of neuronal fates after broad transcription

Given the unexpected finding of *Satb2* mRNA in early-born neural stem cells and overlap with the *Bcl11b* neuronal lineage, we next sought to monitor transcriptional activation of the *Satb2* locus. We employed a fate mapping approach with the *Satb2*$^{Cre/+}$ mouse line [31]. A Cre expression cassette is located in place of exon 2 at the *Satb2* locus, which allows for timed *in utero* electroporation of Cre-inducible reporters like *loxP-STOP-loxP-tdTomato* that clonally labels cells with tdTomato that have a history of *Satb2* transcription (*Satb2*^{tdTom}) (**Fig. 3a**). Co-electroporation with an *eGFP* plasmid serves as a generic label for all transfected cells.

Remarkably, we detected *Satb2*^{tdTom} cells in the ventricular zone as early as E12.5 forming clusters resembling clones or undergoing mitotic divisions (**Fig. 3b**), and express neural

progenitor markers like Pax6 (apical progenitors) or Tbr2 (intermediate progenitors) (**Fig. 3c**). *Satb2* transcription was observed for progenitors in the neocortex, but not in adjacent brain regions (**Extended Data Fig. 3c**). Thus, *Satb2* transcriptional priming occurs in early-born neocortex neural stem cells, indicating broad transcription of a protein expressed in a restricted neuronal lineage appearing later.

The balance of the Bcl11b vs. Satb2 lineages is essential for normal neocortex development and function. Satb2 directly suppresses the *Bcl11b* genomic enhancer, and loss of Satb2 engenders ectopic expression of *Bcl11b* in upper layer neurons, leading to abnormal connectivity [19]. Therefore, we next investigated the expression of Bcl11b and Satb2 protein in cells that transcribe *Satb2* mRNA (**Fig. 3d-e, Supplementary Table 3**). Among cells transcribing *Satb2* mRNA, ~70% express Satb2 protein and ~30% express Bcl11b protein. Taken together, this observation indicates that despite unexpectedly broad and early transcription of the neuronal fate gene *Satb2*, translation of Satb2 protein restricts its expression to a late-born neuronal subtype, and maintains the balance of alternative neuronal fates.

Translation downregulation decreases ribosome levels acutely at mid-neurogenesis E15.5

We next focused on genes that are translationally downregulated across neurogenesis after E12.5. Gene ontology analysis highlighted structural constituents of the ribosome, predominantly ribosomal proteins, as strongly downregulated by translation (**Fig. 4a**). We calculated the developmental expression trajectory of all 79 ribosomal proteins in the large and small subunits by RNA-seq, Ribo-seq, mass spec, and translation efficiency (**Fig. 4b**). Results showed downregulation of nearly all ribosomal proteins at the Ribo-seq and MS level occurs acutely at E15.5, in advance of changes measured by RNA-seq, and reflecting translation downregulation until mid-neurogenesis. Decreasing ribosome levels by downregulation of ribosomal protein translation likely represents the coordinated regulation of this specific gene family, rather than a simple translation feedback loop, since numerous genes in other families undergo translation upregulation concurrently, such as chromatin binding proteins.

To detect changing ribosome numbers sub-cellularly at high resolution, we performed immuno-electron microscopy analysis labeling ribosomal protein uS7 at E12.5 and E15.5 in the

231 neocortex (**Fig. 4c-d and Extended Data Fig. 4, Supplementary Table 3**). A striking
232 decrease in ribosome number was observed in differentiating neurons from early to late stages.
233 Ribosomes are abundant in cortical plate neurons at E12.5, but scarce in both upper and lower
234 layer neurons of the cortical plate at E15.5. Notably, a progressive increase in ribosome
235 number was observed as newly born neurons traverse away from the ventricular zone into the
236 cortical plate at E12.5; while at E15.5, ribosome numbers decrease precipitously outside the
237 ventricular zone, with few ribosomes measured in sub-ventricular zone progenitors. Thus,
238 ribosome number is temporally enforced by translation at mid-gestation. As ribosome
239 abundance is a powerful determinant of translation kinetics and selectivity [32,33], global shifts in
240 translation activity may occur at mid-neurogenesis.
241

242 **Ribosome density at the start codon and within the CDS are developmentally dynamic**

243 We next examined global translation activity during neocortex development by determining
244 ribosome-mRNA interactions per-codon across all coding sequences. Ribosome position
245 aligned to codons in the P-site demonstrated the characteristic 3-nucleotide periodicity in Ribo-
246 seq metagene plots (**Fig. 5a**). We found ribosome occupancy surrounding the start codon
247 increases sharply at E15.5, with progressive increases per stage until P0, while stop codon
248 occupancy demonstrates the opposite trend and occurs independent of start codon changes
249 (**Supplementary Table 4**). We applied RiboDiPA [34], a linear modeling framework designed for
250 positional analysis of Ribo-seq signal, to pinpoint the ~ 5-fold ribosome occupancy changes to
251 the 4 codon bin surrounding the start and stop (**Fig. 5b**).
252

253 Increased ribosome occupancy of the first four codons over time could represent a narrowing
254 bottleneck in the transition from initiation to elongation, or signify increasingly robust initiation
255 of target mRNAs. We correlated fold changes in start codon occupancy with translation
256 efficiency and found an inverse relationship, suggesting that early elongation events
257 progressively slow over time for a large cohort of proteins (**Fig. 5c**). Translation of the N-
258 terminus may become increasingly rate-limiting during synthesis Sbno2 and Pcdhgc4, in
259 contrast to Tuba1c and Tuba1b representing more processive translation during development.
260 Thus, as ribosome levels decline at E15.5 to P0, translation at the 5'-end of coding sequences
261 occurs more slowly.
262

263 We next investigated distinct positions where variations in ribosome density take place [35] (**Fig.**
264 **5d**; see **Methods**). A narrow region consistent with the ribosomal A-site accounts for most of
265 the codon-specific variation in ribosome occupancy. Variation in A-site occupancy was most
266 pronounced at E12.5-E14, with an acute decrease at E15.5-E17, and low variation by P0.
267 Analysis of ribosome dwell time per codon – a measure of the codon-specific speed of
268 translation [36] – demonstrated early developmental "fast" or "slow" kinetics in the bimodal
269 distribution of codon dwell times in the A-site (**Fig. 5e and Extended Data Fig. 5a-b;**
270 **Supplementary Table 4**). At E15.5, codon dwell times begin to equalize, progressively
271 reaching a unimodal distribution by P0. Furthermore, ribosome density occupying A-site
272 codons negatively correlates with P-site density in the embryonic period, but no correlation
273 was measured after birth at P0 (**Fig. 5f**). Thus, the A-site codon in particular influences
274 ribosome dwell time, which is a barrier most pronounced early in neurogenesis when ribosome
275 levels are highest, and less pronounced after mid-neurogenesis when ribosome levels decline.
276

277 Varying ribosome dwell time on a codon might be attributable to the availability of a given
278 tRNA. Dwell time is strongly correlated with tRNA abundance in yeast [37–39], but is less
279 correlated in some mammalian systems [36,40]. We measured levels of 151 tRNA isodecoders by
280 quantitative PCR (qPCR) array at each stage (**Extended Data Fig. 6, Supplementary Table**
281 **4**) to determine if tRNA abundance is responsible for driving ribosome dwell time differences in
282 the developing neocortex. Usage-corrected tRNA abundance (availability) [36] and codon
283 optimality – the non-uniform decoding rate between synonymous codons [41] – failed to show
284 any correlation with ribosome dwell time at the A-site (**Extended Data Fig. 5c-d**).
285

286 However, we found that the amino acid coded for is a strong determinant of ribosome density
287 occupying A-site codons, with synonymous codons showing similar occupancy (**Fig. 5g,**
288 **Supplementary Table 4**). Codons for acidic amino acids are among those with the highest
289 occupancy, suggesting they represent a kinetic barrier in early development translation [38,42].
290 E12.5-E14 accounts for the extremes of A-site differences between amino acids and among
291 synonymous codons, with a progressive, chronologic trend towards equalized occupancy by
292 P0. Notably, some amino acids like leucine and isoleucine are coded for by both "fast" and
293 "slow" synonymous codons, particularly apparent early in development, such as the fast TTA-
294 Leu and slow CTG-Leu. Neither codon optimality (**Extended Data Fig. 5d**) nor codon rarity

295 would account for such dwell time differences, as TTA-Leu is a relatively rare codon [43] with a
296 short dwell time, while CTG-Leu is more common with a long dwell time.
297
298 Taken together, “fast” and “slow” amino acids in the ribosome A-site characterize the early
299 neurogenesis period when ribosome levels are transiently abundant, while ribosome
300 accumulation at the start codon occurs late in neurogenesis when ribosome levels decline (**Fig.**
301 **6a**). These data strongly indicate that the kinetics of translation shift sharply at mid-
302 neurogenesis during a steep decline in ribosome levels, which coincide with major transitions
303 in neuronal fate.
304

305 **The ribosomal protein translation inhibitor eIF4EBP1 impacts neuronal fate and**
306 **migration**

307 The overwhelming influence that changes in ribosome number can have on global protein
308 synthesis kinetics and mRNA-specific translation is strongly supported by theoretical and
309 experimental data [32,33]. However, whether changes in ribosome number (**Fig. 6a**) impact
310 neurogenesis is unknown. We first analyzed mRNAs for sequence motifs in their untranslated
311 regions (UTRs), which are powerful regulators of neocortical translation by RNA-binding
312 proteins [2,14,44]. Distinct motifs are enriched in the 5’- and 3’-UTRs of mRNAs with increasing or
313 decreasing translation efficiency (**Fig. 6b**). Translation downregulation motifs were only
314 detected in 5’-UTRs and are enriched for terminal oligopyrimidine (5’-TOP) sequences. In
315 translation upregulated mRNAs by contrast, 5’ GC-rich sequences and/or 3’ Pumilio binding
316 motifs are prevalent. 5’-TOP sequences are a particular feature of ribosomal proteins coding
317 mRNAs, and lead to their concerted translation downregulation when directly bound by their
318 major upstream regulator eIF4EBP1 (**Fig. 6c**) [20,21]. Since we found that ribosome levels are
319 controlled by a timed decrease in ribosomal protein translation, we next focused on how
320 eIF4EBP1 expression coincides with translation regulation during neocortex development.
321

322 Western blot analysis demonstrated eIF4EBP1 levels change during neocortex development,
323 with high expression at early stages until E15.5, followed by a sharp decrease at E17, and
324 moderate recovery at P0 (**Fig. 6d**). eIF4EBP1 levels coincide with the translation
325 downregulation of ribosomal protein expression measured until E15.5, after which translation
326 inhibition is transiently released at E17 (**Figs. 4b and 6d, bottom**). We next assessed the
327 developmental expression of eIF4EBP1 *in situ* by immunohistochemistry analysis in the

neocortex (**Fig. 6e**). Robust eIF4EBP1 expression was observed in neural stem cells at E12.5-E15.5 in the ventricular zone, with lower expression in cortical plate neurons. At E17, eIF4EBP1 levels decrease throughout both stem cell and neuronal zones, with some recovery at P0. These data suggest eIF4EBP1 may play a role in the early-mid neurogenic period, during a downregulation of ribosomal protein translation, which coincides with an increase in Satb2 translation.

To measure the impact of eIF4EBP1 on neuronal fate during neocortex neurogenesis, we performed shRNA knockdown by *in utero* electroporation in ventricular zone progenitors at E13.5 when eIF4EBP1 levels are high, followed by immunohistochemistry assessment of Satb2 protein expression at E15.5 when translation regulation dynamics peak (**Fig. 6f**). eIF4EBP1 knockdown in early progenitors leads to a decrease in the fraction of Satb2 protein expressing neurons at E15.5 compared to scrambled control, and arrests neuronal entry into the cortical plate (**Fig. 6f-g, Supplementary Table 3**). These data indicate that eIF4EBP1 impacts neuronal fate and migration during a large-scale transient shift in translation activity at mid-gestation.

Taken together, our data supports a model where E15.5 is a major inflection point in translation regulation during neocortex neurogenesis (**Fig. 6h**). This critical window includes a robust decrease in ribosome number in differentiating neurons, a change in translation kinetics, and global shifts in the translation efficiency of mRNAs – including genes driving neuronal specification.

Modeling the translatome of neocortex neurogenesis

Having interrogated members of the most translationally upregulated and downregulated gene pathways, we pursued a more comprehensive bioinformatic analysis of the transcriptome-to-proteome transition in coordinated developmental programs – where deviations between mRNA and protein may represent dynamic cellular transitions [1]. We performed hierarchical clustering of mRNA and protein expression trajectories after E12.5 per gene, which divided the proteome into 13 broad clusters (**Fig. 7a and Extended Data Fig. 7a, Supplementary Table 5**). We found clusters representing concordant and divergent trajectories between mRNA and protein, with E15.5 a common inflection point of divergent regulation. While genes with changing translation efficiency are found in all clusters, they are enriched in clusters that

361 demonstrate highly divergent mRNA and protein expression. Furthermore, several essential
362 neural stem cell and differentiation markers segregate into distinct clusters, such as *Nes* in
363 cluster J and *Satb2* in cluster M. Reinforcing the biological significance of clusters representing
364 different mRNA and protein trajectories, gene ontology analysis demonstrated many non-
365 overlapping, distinct pathways enriched in different clusters, such as neuron differentiation
366 processes enriched in cluster D (**Fig. 7b, Supplementary Table 5**).
367
368 The relationship between Ribo-seq density and steady state protein levels is complicated by
369 the fact that protein half-lives are relatively long [45], and reflect the cumulative effects of
370 synthesis and degradation over time. In contrast, Ribo-seq reflects synthesis at a given time
371 point. Deviations between protein and Ribo-seq are expected whenever protein levels have not
372 yet reached equilibrium with synthesis, making linear comparison of protein concentrations and
373 Ribo-seq densities difficult to interpret. We therefore made use of a kinetic, time continuous
374 model of protein translation similar to [46] (see **Methods**).
375
376 We classified proteins into one of five categories (**Fig. 7c**): *stationary*, where protein levels
377 showed little change; *linear*, where protein levels were in near-equilibrium with Ribo-seq
378 measured synthesis; *production*, consistent with a non-equilibrium protein trajectory;
379 *degradation*, for which protein degradation alone fit the data; and *"MSdev"*, whose protein
380 trajectories diverged from their Ribo-seq trajectory for any combination of parameters. Then,
381 by using the approximation of single constant relating RPF density and synthesis rate, we were
382 able to estimate half-lives for all genes, which show a strong correlation to experimentally
383 determined degradation rates in NIH 3T3 cells [47] (**Extended Data Fig. 7b**). For example, our
384 predicted MSdev category proteins are more likely to demonstrate non-exponential decay
385 kinetics during their lifetime (**Extended Data Fig. 7c**).
386
387 Genes in the five modeled categories showed distinct gene ontology term enrichment (**Fig. 7d**),
388 such as the linear relationship between the translation and abundance of ribosome
389 components, or the non-linear relationship for chromatin associated proteins. Interestingly, G-
390 protein coupled receptors and DNA replication genes are enriched in the MSdev category,
391 suggesting their expression patterns are highly multifaceted. In contrast, transmembrane
392 transporter protein levels are highly stable, buffering upstream transcription/translation

393 changes. Thus, our modeling highlights how multiple layers of post-transcriptional regulation
394 impact distinct gene families during the time course of neuronal differentiation.
395

396 **Discussion**

397 Our study traces how functional gene expression is catalyzed in a complex developmental
398 system, capturing the reactants, synthesis, and products of mRNA translation across the time
399 course of neocortex neurogenesis. We find widespread deviations in the trajectory of mRNA
400 and protein expression along with changes in translation for ~18% of the transcriptome, with a
401 transient peak at mid-neurogenesis. We interrogate the protein families most enriched among
402 translation up and downregulated genes. Translation upregulation particularly impacts
403 chromatin binding proteins like Satb2, which are essential components of neurogenesis.
404 Translation downregulation targets the translation machinery itself, with an acute decline in
405 ribosome number at mid-neurogenesis. The transition from relative ribosome abundance to
406 depletion is accompanied by a chronological shift in translation processivity at the start codon
407 and A-site amino acid during peptide elongation. eIF4EBP1, the major upstream suppressor of
408 ribosomal protein translation efficiency, is dynamically expressed during neurogenesis in
409 tandem with ribosome abundance, and impacts Satb2 neuronal fate specification. Finally, we
410 model the transcriptome-to-proteome transition in neocortex development, highlighting the
411 impact of translation in a multilayered program of neurodevelopmental gene expression.
412

413 Neural stem cells and differentiated neurons harbor a pool of mRNAs inclusive of diverse
414 neuronal fates [4,7]. We propose that a broad transcriptome is filtered at the protein level for
415 tightly timed, rapidly scalable, and spatially targeted gene expression to assemble highly
416 evolved neuronal circuits. Per gene per hour, translation is faster and more scalable than
417 transcription by orders of magnitude [48], and neuronal specification transitions occur in very
418 narrow developmental windows [2,3]. The availability of a diverse mRNA repertoire including
419 both lower and upper layer neuronal fates like *Bcl11b* and *Satb2*, respectively, which can be
420 rapidly and selectively amplified by translation upregulation, is essential to specify Bcl11b or
421 Satb2 protein exclusive neurons, in addition to Bcl11b-Satb2 double-positive neurons [6]. Our
422 translatome data provide a unique window into how the proteome emerges from the
423 transcriptome in neurodevelopment (https://shiny.mdc-berlin.de/cortexomics/).
424

425 The timed decrease in ribosome number per cell in the cortical plate represents a coordinated
426 translation downregulation of ribosomal protein synthesis. Control of ribosome number has a
427 dominant influence on global protein synthesis kinetics and mRNA-specific translation, and can
428 lead to "ribosomopathies" in disease states [32,33]. With the role of eIF4EBP1 early in
429 neurogenesis, our study joins an evolving body of work on RNA-binding proteins and ribosome
430 cofactors that modulate protein synthesis in the developing brain [2,5,13–16,44]. eIF4EBP1 is a
431 master regulator of ribosome levels by suppressing ribosomal protein synthesis [20,21], which we
432 find also impacts the fate and migration of a neuronal lineage prenatally. A timed mechanism
433 to finely tune ribosome levels may impose essential control on how and when proteins are
434 synthesized during neuronal fate decisions.
435
436 We measure a timed, progressive developmental shift in ribosome density surrounding start
437 and stop codons. Previous studies of the "5' ramp" present in Ribo-seq experiments have
438 proposed that it represents 'slow' synonymous codon choice near the coding sequence start –
439 an adaptation to prevent ribosome collision further into the open reading frame [49]. Our data
440 argue against this as the sole mechanism of 5' ramping, since numerous genes show an
441 increase in start density despite the generally decreasing effect of codon choice. The
442 increasing relative density at the 5' of many mRNA coding sequences resembles what might
443 be expected during a shift from ribosome abundant elongation-limited to ribosome scarce
444 initiation-limited translation [50], when kinetic barriers to start codon initiation and elongation of
445 early N-terminal peptides [51] become comparatively prominent. Of note, we do not observe
446 increasing start codon density only for high translation efficiency genes, or correlation with
447 neurite-localized translation (**Extended Data Fig. 8**). We therefore favor the hypothesis that
448 ribosome occupancy at beginning of open reading frames becomes progressively rate-limiting
449 for codon-independent reasons, such as scarcity of translation cofactors and ribosomal
450 subunits later in development.
451
452 We also find that the A-site amino acid strongly influences translation speed during early
453 neurogenesis in particular, suggesting that factors like the electrostatics of peptidyl chain
454 elongation [38,42], amino acid availability, and/or tRNA aminoacylation might play a more
455 important role in early brain development. To our knowledge, our study is the first to
456 demonstrate differences in the fundamental nature of codon-specific ribosome density over
457 developmental time. Our study agrees with previous work that suggest tRNA levels are not a

limiting factor for translation elongation in mammals [36,40,52], as they are in exponentially dividing yeast [37–39]. Notably, however, these findings do not rule out individual cases where a tRNA may influence ribosome stalling, as reported for one nervous system-specific tRNA postnatally [53]. We measure the total tRNA pool with a protocol that does not address tRNA charging, which is a limitation of our study and an interesting future direction for investigation.

The main limitation of our study is that parallel time course measurements of the transcriptome, tRNA pool, translatome, and proteome occur in brain tissue of mixed cell types rather than single cells. In addition to scRNA-seq, tremendous advances in analysis of the single-cell translatome by Ribo-seq [54] were just published. While development of single-cell proteomics is still underway [55,56], the input requirements for tRNA measurement remain a major obstacle. At the expense of cellular resolution, we opted to perform a comprehensive analysis that enables modeling of mRNA translation in developing brain tissue. Notably, while our study is well designed to measure changes in protein synthesis, we do not measure protein degradation directly. The unexpectedly large number of “MSdev” proteins identified in our model indicates that post-translational mechanisms like degradation [57–59] may also have a major impact by decoupling protein and Ribo-seq trajectories, highlighting the complexity of gene regulation in the neocortex. Despite these limitations, our approach detected two important phenomena validated at the cell type-specific level – mRNA-protein uncoupling of Satb2 by translation upregulation, and coordinated translation downregulation of ribosome abundance. Bulk tissue measurements can be very informative in tandem with single cell data deconvolution in the brain [60–62], and we anticipate our data will be leveraged as more single cell technologies emerge.

Taken together, our data suggests a model of developmental gene expression where the levels and kinetics of translation shift during a key window of neurogenesis in the brain – creating a major inflection point of translation at mid-gestation. These developmental windows correspond to timed changes in neuronal specification from neural stem cells, where broad transcription of neuronal subtype-specific programs is ultimately refined by translational control, more precisely demarcating the boundaries of neuronal circuits in the brain.

Acknowledgements

We thank Nadja Klein for advice regarding modeling and statistics, and Heike Heilmann for support with immuno-electron microscopy. M.L.K. would like to thank Martin Vingron for support. M.L.K. was funded by an EMBO Long-Term Postdoctoral Fellowship (190-2016), Alexander von Humboldt Foundation Postdoctoral Fellowship, and International Guest Fellowship from the Max Planck Institute for Molecular Genetics. D.H. was supported by a grant from the Klaus Tschira Boost Fund. *In utero* electroporation experiments were funded by a Russian Science Foundation Basic Research grant (19-34-51009) to V.T.

Author Contributions

M.L.K. designed and initiated the study, with D.H. and M.C.A. making essential contributions. U.O. and V.T. supervised the study, with contributions from C.M.T.S., M.L., M.S., and T.M. Computational experiments were performed by D.H., and laboratory experiments by M.C.A., M.L.K., A.R., E.B., and R.D. Ribo-seq and RNA-seq sample preparation and sequencing were performed by U.Z. and M.L.K., and mass spectrometry sample preparation and measurement by K.I. and M.L.K. Immuno-electron microscopy samples were prepared by A.M.-W. and imaged by B.F. and M.L.K. Data were interpreted by D.H., M.C.A., and M.L.K. Manuscript figures and text were composed by D.H., M.C.A., and M.L.K., with valuable editing and input from all authors.

Competing Interests

The authors declare no competing interests.

References

1. Buccitelli, C. & Selbach, M. mRNAs, proteins and the emerging principles of gene expression control. *Nat. Rev. Genet.* **21**, 630–644 (2020).

2. DeBoer, E. M., Kraushar, M. L., Hart, R. P. & Rasin, M. R. Post-transcriptional regulatory elements and spatiotemporal specification of neocortical stem cells and projection neurons. *Neuroscience* **248**, 499–528 (2013).

3. Cadwell, C. R., Bhaduri, A., Mostajo-Radji, M. A., Keefe, M. G. & Nowakowski, T. J. Development and Arealization of the Cerebral Cortex. *Neuron* **103**, 980–1004 (2019).

4. Telley, L. *et al.* Temporal patterning of apical progenitors and their daughter neurons in the developing neocortex. *Science.* **364**, (2019).

5. Zahr, S. K. *et al.* A Translational Repression Complex in Developing Mammalian Neural Stem Cells that Regulates Neuronal Specification. *Neuron* **97**, 520–537 (2018).

6. Nowakowski, T. J. *et al.* Spatiotemporal gene expression trajectories reveal developmental hierarchies of the human cortex. *Science.* **358**, 1318–1323 (2017).

7. Klingler, E. *et al.* Temporal controls over inter-areal cortical projection neuron fate diversity. *Nature* **599**, 453–457 (2021).

8. Llorca, A. *et al.* A stochastic framework of neurogenesis underlies the assembly of neocortical cytoarchitecture. *Elife* **8**, e51381 (2019).

9. Klingler, E. & Jabaudon, D. Do progenitors play dice? *Elife* **9**, e54042 (2020).

10. Hoye, M. L. & Silver, D. L. Decoding mixed messages in the developing cortex: translational regulation of neural progenitor fate. *Curr. Opin. Neurobiol.* **66**, 93–102 (2021).

11. Kraushar, M. L., Popovitchenko, T., Volk, N. L. & Rasin, M.-R. The frontier of RNA metamorphosis and ribosome signature in neocortical development. *Int. J. Dev. Neurosci.* **55**, 131–139 (2016).

12. Kraushar, M. L. *et al.* Thalamic WNT3 Secretion Spatiotemporally Regulates the Neocortical Ribosome Signature and mRNA Translation to Specify Neocortical Cell Subtypes. *J. Neurosci.* **35**, 10911–10926 (2015).

13. Kraushar, M. L. *et al.* Temporally defined neocortical translation and polysome assembly are determined by the RNA-binding protein Hu antigen R. *Proc. Natl. Acad. Sci. USA* **111**, E3815-24 (2014).

14. Zahr, S. K., Kaplan, D. R. & Miller, F. D. Translating neural stem cells to neurons in the mammalian brain. *Cell Death Differ.* **26**, 2495–2512 (2019).

15. Kraushar, M. L. *et al.* Protein Synthesis in the Developing Neocortex at Near-Atomic Resolution Reveals Ebp1-Mediated Neuronal Proteostasis at the 60S Tunnel Exit. *Mol. Cell* **81**, 304-322.e16 (2021).

16. Popovitchenko, T. *et al.* Translational derepression of Elavl4 isoforms at their alternative 5′ UTRs determines neuronal development. *Nat. Commun.* **11**, 1674 (2020).

17. Kalish, B. T. *et al.* Maternal immune activation in mice disrupts proteostasis in the fetal brain. *Nat. Neurosci.* **24**, 204–13 (2021).

18. Ingolia, N. T., Ghaemmaghami, S., Newman, J. R. S. & Weissman, J. S. Genome-wide analysis in vivo of translation with nucleotide resolution using ribosome profiling. *Science.* **324**, 218–223 (2009).

19. Britanova, O. *et al.* Satb2 Is a Postmitotic Determinant for Upper-Layer Neuron Specification in the Neocortex. *Neuron* **57**, 378–392 (2008).

20. Thoreen, C. C. *et al.* A unifying model for mTORC1-mediated regulation of mRNA translation. *Nature* **485**, 109–13 (2012).

21. Jin, H. *et al.* TRIBE editing reveals specific mRNA targets of eIF4E-BP in Drosophila and in mammals. *Sci. Adv.* **6**, eabb8771 (2020).

561 22. Greig, L. C., Woodworth, M. B., Galazo, M. J., Padmanabhan, H. & Macklis, J. D.
562 Molecular logic of neocortical projection neuron specification, development and diversity.
563 *Nat. Rev. Neurosci.* **14**, 755–69 (2013).

564 23. Ingolia, N. T. Ribosome Footprint Profiling of Translation throughout the Genome. *Cell*
565 **165**, 22–33 (2016).

566 24. Dunn, J. G., Foo, C. K., Belletier, N. G., Gavis, E. R. & Weissman, J. S. Ribosome
567 profiling reveals pervasive and regulated stop codon readthrough in Drosophila
568 melanogaster. *Elife* **2**, 1–32 (2013).

569 25. Li, J. J., Bickel, P. J. & Biggin, M. D. System wide analyses have underestimated protein
570 abundances and the importance of transcription in mammals. *PeerJ* **2**, e270 (2014).

571 26. Jovanovic, M. *et al.* Dynamic profiling of the protein life cycle in response to pathogens.
572 *Science.* **347**, 1259038 (2015).

573 27. Arlotta, P. *et al.* Neuronal subtype-specific genes that control corticospinal motor neuron
574 development in vivo. *Neuron* **45**, 207–21 (2005).

575 28. Alcamo, E. a. *et al.* Satb2 Regulates Callosal Projection Neuron Identity in the
576 Developing Cerebral Cortex. *Neuron* **57**, 364–377 (2008).

577 29. Frederikson, K. & McKay, R. D. G. Proliferation and differentiation of rat neuroepithelial
578 precursor cells in vivo. *J. Neurosci.* **8**, 1144–1151 (1988).

579 30. Josephson, R. *et al.* POU transcription factors control expression of CNS stem cell-
580 specific genes. *Development* **125**, 3087–3100 (1998).

581 31. Ambrozkiewicz, M. C., Bessa, P., Salazar-Lázaro, A., Salina, V. & Tarabykin, V. Satb2
582 Cre/+ mouse as a tool to investigate cell fate determination in the developing neocortex.
583 *J. Neurosci. Methods* **291**, 113–121 (2017).

584 32. Mills, E. W. & Green, R. Ribosomopathies: There's strength in numbers. *Science.* **358**,
585 eaan2755 (2017).

586 33. Shah, P., Ding, Y., Niemczyk, M., Kudla, G. & Plotkin, J. B. Rate-limiting steps in yeast
587 protein translation. *Cell* **153**, 1589–1601 (2013).

588 34. Li, K., Hope, C. M., Wang, X. A. & Wang, J. P. RiboDiPA: a novel tool for differential
589 pattern analysis in Ribo-seq data. *Nucleic Acids Res.* **48**, 12016–12029 (2020).

590 35. O'Connor, P. B. F., Andreev, D. E. & Baranov, P. V. Comparative survey of the relative
591 impact of mRNA features on local ribosome profiling read density. *Nat. Commun.* **7**,
592 12915 (2016).

593 36. Gobet, C. *et al.* Robust landscapes of ribosome dwell times and aminoacyl-tRNAs in
594 response to nutrient stress in liver. *Proc. Natl. Acad. Sci. U. S. A.* **117**, 9630–9641
595 (2020).

596 37. Fang, H. *et al.* Scikit-ribo Enables Accurate Estimation and Robust Modeling of
597 Translation Dynamics at Codon Resolution. *Cell Syst.* **6**, 180-191.e4 (2018).

598 38. Riba, A. *et al.* Protein synthesis rates and ribosome occupancies reveal determinants of
599 translation elongation rates. *Proc. Natl. Acad. Sci.* **116**, 15023–15032 (2019).

600 39. Weinberg, D. E. *et al.* Improved Ribosome-Footprint and mRNA Measurements Provide
601 Insights into Dynamics and Regulation of Yeast Translation. *Cell Rep.* **14**, 1787–1799
602 (2016).

603 40. Ingolia, N. T., Lareau, L. F. & Weissman, J. S. Ribosome profiling of mouse embryonic
604 stem cells reveals the complexity and dynamics of mammalian proteomes. *Cell* **147**,
605 789–802 (2011).

606 41. dos Reis, M., Savva, R. & Wernisch, L. Solving the riddle of codon usage preferences: A
607 test for translational selection. *Nucleic Acids Res.* **32**, 5036–5044 (2004).

608 42. Chadani, Y. *et al.* Intrinsic Ribosome Destabilization Underlies Translation and Provides
609 an Organism with a Strategy of Environmental Sensing. *Mol. Cell* **68**, 528–539 (2017).

610 43. Quax, T. E. F., Claassens, N. J., Söll, D. & van der Oost, J. Codon Bias as a Means to
611 Fine-Tune Gene Expression. *Mol. Cell* **59**, 149–161 (2015).

612 44. Lennox, A. L., Mao, H. & Silver, D. L. RNA on the brain: emerging layers of post-
613 transcriptional regulation in cerebral cortex development. *WIREs Dev. Biol.* **7**, e290
614 (2018).

615 45. Schwanhäusser, B. *et al.* Global quantification of mammalian gene expression control.
616 *Nature* **473**, 337–42 (2011).

617 46. Becker, K. *et al.* Quantifying post-transcriptional regulation in the development of
618 Drosophila melanogaster. *Nat. Commun.* **9**, 4970 (2018).

619 47. McShane, E. *et al.* Kinetic Analysis of Protein Stability Reveals Age-Dependent
620 Degradation. *Cell* **167**, 803-815.e21 (2016).

621 48. Schwanhäusser, B., Gossen, M., Dittmar, G. & Selbach, M. Global analysis of cellular
622 protein translation by pulsed SILAC. *Proteomics* **9**, 205–209 (2009).

623 49. Pechmann, S. & Frydman, J. Evolutionary conservation of codon optimality reveals
624 hidden signatures of cotranslational folding. *Nat. Struct. Mol. Biol.* **20**, 237–243 (2013).

625 50. Heyer, E. E. & Moore, M. J. Redefining the Translational Status of 80S Monosomes. *Cell*
626 **164**, 757–769 (2016).

627 51. Verma, M. *et al.* A short translational ramp determines the efficiency of protein synthesis.
628 *Nat. Commun.* **10**, 5774 (2019).

629 52. Gingold, H. *et al.* A dual program for translation regulation in cellular proliferation and
630 differentiation. *Cell* **158**, 1281–1292 (2014).

631 53. Ishimura, R. *et al.* Ribosome stalling induced by mutation of a CNS-specific tRNA
632 causes neurodegeneration. *Science.* **345**, 455–9 (2014).

633 54. Vaninsberghe, M., Berg, J., Andersson-rolf, A., Clevers, H. & Oudenaarden, A. Single-
634 cell Ribo-seq reveals cell cycle-dependent translational pausing. *Nature* **597**, 561–565

635 (2021).

636 55. Slavov, N. Unpicking the proteome in single cells. *Science.* **367**, 512–513 (2020).

637 56. Brunner, A.-D. *et al.* Ultra-high sensitivity mass spectrometry quantifies single-cell
638 proteome changes upon perturbation. *bioRxiv* (2020). doi:10.1101/2020.12.22.423933

639 57. Ambrozkiewicz, M. C. & Kawabe, H. HECT-type E3 ubiquitin ligases in nerve cell
640 development and synapse physiology. *FEBS Lett.* **589**, 1635–1643 (2015).

641 58. Chiang, S. Y. *et al.* Usp11 controls cortical neurogenesis and neuronal migration through
642 Sox11 stabilization. *Sci. Adv.* **7**, eabc6093 (2021).

643 59. Ambrozkiewicz, M. C. *et al.* Polarity Acquisition in Cortical Neurons Is Driven by
644 Synergistic Action of Sox9-Regulated Wwp1 and Wwp2 E3 Ubiquitin Ligases and
645 Intronic miR-140. *Neuron* **100**, 1097-1115.e15 (2018).

646 60. Wang, X., Park, J., Susztak, K., Zhang, N. R. & Li, M. Bulk tissue cell type deconvolution
647 with multi-subject single-cell expression reference. *Nat. Commun.* **10**, (2019).

648 61. Jew, B. *et al.* Accurate estimation of cell composition in bulk expression through robust
649 integration of single-cell information. *Nat. Commun.* **11**, 1971 (2020).

650 62. Harris, B. D., Crow, M., Fischer, S. & Gillis, J. Single-cell co-expression analysis reveals
651 that transcriptional modules are shared across cell types in the brain. *Cell Syst.* **12**, 748-
652 756.e3 (2021).

653 63. Martin, M. Cutadapt removes adapter sequences from high-throughput sequencing
654 reads. *EMBnet.journal* **17**, 10–11 (2011).

655 64. Langmead, B. & Salzberg, S. L. Fast gapped-read alignment with Bowtie 2. *Nat.*
656 *Methods* **9**, 357–359 (2012).

657 65. Dobin, A. *et al.* STAR: ultrafast universal RNA-seq aligner. *Bioinformatics* **29**, 15–21
658 (2013).

659 66. Law, C. W., Chen, Y., Shi, W. & Smyth, G. K. Voom: Precision weights unlock linear
660 model analysis tools for RNA-seq read counts. *Genome Biol.* **15**, R29 (2014).

661 67. Xiao, Z., Zou, Q., Liu, Y. & Yang, X. Genome-wide assessment of differential translations
662 with ribosome profiling data. *Nat. Commun.* **7**, 1–11 (2016).

663 68. Calviello, L., Sydow, D., Harnett, D. & Ohler, U. Ribo-seQC: comprehensive analysis of
664 cytoplasmic and organellar ribosome profiling data. *bioRxiv* (2019). doi:10.1101/601468

665 69. Ahmed, N. *et al.* Identifying A- and P-site locations on ribosome-protected mRNA
666 fragments using Integer Programming. *Sci. Rep.* **9**, 6256 (2019).

667 70. Cui, H., Hu, H., Zeng, J. & Chen, T. DeepShape: Estimating isoform-level ribosome
668 abundance and distribution with Ribo-seq data. *BMC Bioinformatics* **20**, 678 (2019).

669 71. Patro, R., Duggal, G., Love, M. I., Irizarry, R. A. & Kingsford, C. Salmon provides fast
670 and bias-aware quantification of transcript expression. *Nat. Methods* **14**, 417–419 (2017).

671 72. Köster, J. & Rahmann, S. Snakemake - a scalable bioinformatics workflow engine.
672 *Bioinformatics* **28**, 2520–2522 (2012).

673 73. Soneson, C., Love, M. I. & Robinson, M. D. Differential analyses for RNA-seq:
674 Transcript-level estimates improve gene-level inferences. *F1000Research* **4**, 1–19
675 (2016).

676 74. Cox, J. & Mann, M. MaxQuant enables high peptide identification rates, individualized
677 p.p.b.-range mass accuracies and proteome-wide protein quantification. *Nat. Biotechnol.*
678 **26**, 1367–1372 (2008).

679 75. Cox, J. *et al.* Andromeda: A peptide search engine integrated into the MaxQuant
680 environment. *J. Proteome Res.* **10**, 1794–1805 (2011).

681 76. Cox, J. *et al.* Accurate Proteome-wide Label-free Quantification by Delayed
682 Normalization and Maximal Peptide Ratio Extraction, Termed MaxLFQ. *Mol. Cell.*
683 *Proteomics* **13**, 2513–2526 (2014).

684 77. McLeay, R. C. & Bailey, T. L. Motif Enrichment Analysis: A unified framework and an
685 evaluation on ChIP data. *BMC Bioinformatics* **11**, 165 (2010).

686 78. Ray, D. *et al.* A compendium of RNA-binding motifs for decoding gene regulation. *Nature*
687 **499**, 172–177 (2013).

688 79. Schindelin, J. *et al.* Fiji: An open-source platform for biological-image analysis. *Nat.*
689 *Methods* **9**, 676–682 (2012).

690 80. Ambrozkiewicz, M. C. *et al.* The murine ortholog of Kaufman oculocerebrofacial
691 syndrome protein Ube3b regulates synapse number by ubiquitinating Ppp3cc. *Mol.*
692 *Psychiatry* **26**, 1980–1995 (2020).

693 81. Zappulo, A. *et al.* RNA localization is a key determinant of neurite-enriched proteome.
694 *Nat. Commun.* **8**, 583 (2017).

695

Methods

Mice

Mouse (*Mus musculus*) lines were maintained in the animal facilities of the Charité University Hospital and Lobachevsky State University. All experiments were performed in compliance with the guidelines for the welfare of experimental animals approved by the State Office for Health and Social Affairs, Council in Berlin, Landesamt für Gesundheit und Soziales (LaGeSo), permissions T0267/15, G0079/11, G206/16, and G54/19, and by the Ethical Committee of the Lobachevsky State University of Nizhny Novgorod. Mice were utilized in the embryonic (E12.5-E17) and early post-natal (P0) period, inclusive of both male and female sexes in each litter without distinction. Timed pregnant wild-type (WT) CD-1 mice utilized for Ribo-seq, RNA-seq, tRNA qPCR array, mass spectrometry, and immuno-electron microscopy were obtained from the Charles River Company (Protocol: T0267/15). Experiments with fluorescent *in situ* hybridization and immunohistochemistry were performed in NMRI WT mice. For experiments with the tdTomato reporter, *Satb2*$^{Cre/+}$ males [19] were mated to NMRI wild type females (Protocols: G0079/11, G54/19, and G206/16). *Satb2*$^{Cre/+}$ mouse genotyping was performed as described [19].

Neocortex sample preparation for bioinformatics analysis

Dissection, cryogenic lysis, and determination of optical density units (ODU) were performed as described [15].

Ribo-seq and RNA-seq sample preparation and sequencing

Each replicate for paired neocortex Ribo-seq and RNA-seq included 40 brains (80 hemispheres) at E12.5, 30 brains (60 hemispheres) at E14, 21 brains (42 hemispheres) at E15.5, 20 brains (40 hemispheres) at E17, and 17 brains (34 hemispheres) at P0 – performed in biological duplicate at each stage. Neocortex tissue was lysed on ice in 20 mM HEPES, 100 mM KCl, 7.5 mM $MgCl_2$, pH 7.4, supplemented with 20 mM Dithiothreitol (DTT), 0.04 mM Spermine, 0.5 mM Spermidine, 1x Protease Inhibitor cOmplete EDTA-free (Roche, 05056489001), 0.3% v/v IGEPAL CA-630 detergent (Sigma, I8896) and clarified by centrifugation at 16100 x*g* for 5 min at 4 °C with a benchtop centrifuge. Samples were then measured for A260 ODU on a NanoDrop 1000 Spectrophotometer. Two thirds of the sample were transferred to a new tube for Ribo-seq preparation, with the remaining one third for RNA-

728 seq was mixed with 100 U SUPERase-In RNAse inhibitor (ThermoFisher, AM2694) and frozen
729 at -80 °C for downstream RNA isolation.
730
731 For digestion of ribosome protected RNA fragments (RPFs), Ribo-seq samples were then
732 mixed with 60U RNAse-T1 plus 96 ng RNAse-A per ODU, and incubated for 30 min at 25 °C,
733 shaking at 400 rpm. To stop RNAse activity, 200 U of SUPERase-In RNAse inhibitor was then
734 added.
735
736 10-50 % 5 mL sucrose density gradients were prepared in Beckman Coulter Ultra-Clear Tubes
737 (344057). Base buffer consisted of 20 mM HEPES, 100 mM KCl, 10 mM $MgCl_2$, 20 mM
738 Dithiothreitol (DTT), 0.04 mM Spermine, 0.5 mM Spermidine, 1x Protease Inhibitor cOmplete
739 EDTA-free (Roche, 05056489001), 20 U/mL SUPERase-In RNAse inhibitor (ThermoFisher,
740 AM2694), pH 7.4, prepared with 10 & 50 % sucrose w/v. Overlaid 10 & 50 % sucrose-buffer
741 solutions were mixed to linearized gradients with a BioComp Gradient Master 107ip.
742
743 Digested lysates were overlaid on gradients pre-cooled to 4 °C. Gradients were centrifuged in
744 a SW55 rotor (Beckman Coulter) for 1 hr, 4 °C, 37000 rpm, and fractionated using a BioComp
745 Piston Gradient Fractionator and Pharmacia LKB SuperFrac, with real-time A260
746 measurement by an LKB 22238 Uvicord SII UV detector recorded using an ADC-16
747 PicoLogger and associated PicoLogger software. Fractions corresponding digested 80S
748 monosomes were pooled and stored at -80 °C.
749
750 RNA isolation with TRIzol LS was then performed for both RNA-seq and Ribo-seq samples, as
751 per the manufacturer's instructions. For Ribo-seq and RNA-seq samples, downstream library
752 preparation and sequencing were performed as described [15]. RNA-seq data were utilized in a
753 recent study [15] corresponding to NIH GEO entry GSE157425. Ribo-seq data in this study are
754 deposited in the NIH GEO: GSE169457.
755
756 **Mass spectrometry sample preparation**
757 Total proteome analysis from neocortex lysates at E12.5, E14, E15.5, E17, and P0, including
758 complete lysis in RIPA buffer, and downstream processing for mass spectrometry analysis,
759 was performed in a recent study [15] corresponding to ProteomeXchange entry PXD014841.
760

761 **tRNA qPCR array sample preparation and measurement**

762 tRNA qPCR array measurement of 151 tRNA isodecoders was performed by Arraystar
763 (Maryland, USA) for neocortex lysates at E12.5, E14, E15.5, E17, and P0 from the same total
764 RNA isolated for RNA-seq described above (**Supplementary Table 4**). Data are deposited in
765 the NIH GEO: GSE169621.

766

767 **Ribo-seq and RNA-seq data processing**

768 Raw sequence data was converted to FASTQ format using bcl2fastq
769 (https://support.illumina.com/downloads/bcl2fastq-conversion-software-v2-20.html). Adapters
770 (sequence TGGAATTCTCGGGTGCCAAGG) were removed from Ribo-seq reads with
771 cutadapt [63], as well as sequences with a quality score less than 20 or a remaining sequence
772 length less than 12, and after removing duplicate read sequences, 4bp UMIs were trimmed
773 from either end of each sequence using a custom perl script. Ribo-seq reads were then
774 aligned to an index of common contaminants (including tRNA, rRNA, and snoRNA sequences)
775 using bowtie2 [64]. The resulting processed read files were then aligned to coding sequences
776 (the pc_transcripts fasta file), and separately, to the genome, from GENCODE release M12
777 (*Mus musculus*) using STAR [65], with the following settings: STAR --outSAMmode NoQS --
778 outSAMattributes NH NM --seedSearchLmax 10 --outFilterMultimapScoreRange 0 --
779 outFilterMultimapNmax 255 --outFilterMismatchNmax 1 --outFilterIntronMotifs
780 RemoveNoncanonical. RNA-seq and Ribo-seq libraries achieved high coverage, with a median
781 of 33M and 12M reads mapped to protein coding transcripts, respectively. For quality control,
782 downstream analysis focused on coding sequences with 32 or more Ribo-seq footprints in at
783 least one stage as per [24], which resulted in a set of 12,228 translated gencode transcripts
784 (**Supplementary Table 1**).

785

786 Linear fold changes for RNA-seq and Ribo-seq were calculated using limma [66], for TE was
787 calculated using xtail [67], and for MS calculated using proDA (https://github.com/const-
788 ae/proDA) (**Supplementary Table 2**).

789

790 Since ribosomes with their A-site over a given position will produce a distribution of read
791 lengths mapping to nearby positions, A/P-site alignment represents a crucial step in the
792 processing of Ribo-seq datasets. Frequently, algorithms for A-site alignment rely either
793 explicitly [37,68] or implicitly (Ahmed et al., 2019;) on the presence of large peaks at the start

794 and/or stop codons, the known location of which provides a 'true positive' that can be used to
795 choose P-site offsets for each read length. We found that such methods gave inconsistent
796 results in our data, with optimal P-sites being chosen at biochemically implausible values (e.g.,
797 at 0 base pairs from the read 5'-end). This is likely due to 1) the variable occupancy of the
798 start/stop peak in our data, and 2) the presence of cut-site bias in our data due to the necessity
799 of RNAse T1 & A digestion. Calculating RUST scores and 'metacodon' [35] plots of RPF 5'-end
800 occurrence showed that the most variation between different codons and time points (other
801 than cut-site bias itself at RPF termini) was nonetheless limited to a narrow region a consistent
802 distance from the codon, for each read length. Plotting KL-Divergence between observed and
803 expected RUST scores at different distances from the read 5' end and measuring the between-
804 codon variance at each position revealed that it aligned with an offset of approximately 14-15
805 nt (consistent with the A-site position) for reads of length between 25 and 31, and so we chose
806 these for further analysis of ribosome dwell time (**Supplementary Table 4**). We also observed
807 an adjacent region of lesser variability 3bp towards the RPF 5' end, consistent with a non-zero
808 but significantly less influence of the P-site codon (**Supplementary Table 4**).
809
810 The program DeepShapePrime [70], modified to accept our chosen P-site offsets instead of
811 hardcoded ones, was then used to derive isoform specific abundance measurements for each
812 protein coding transcript.
813
814 In parallel to the above, iso-form level quantification of the RNA-seq was carried out using
815 salmon [71], with an index built from coding M12 sequences, and the following settings: salmon
816 quant -l SR --seqBias --validateMappings
817
818 A snakemake [72] file automating the above workflow is available at:
819 https://github.com/ohlerlab/cortexomics.
820
821 We then converted DeepShape-prime's output to salmon format to combine both outputs,
822 using the ORF length as effective length. The R package tximport [73] was used to derive length-
823 corrected gene-level counts and isoform level counts and TPMs for both datasets. The voom
824 package was used for variance stabilization and linear modelling of this data to derive
825 confidence intervals for transcriptional and translational change, both relative to E12.5, and
826 stepwise between each stage. The xtail package [67], which is specifically geared towards

827 estimation of translational efficiency (TE; i.e. the ratio of Ribo-seq density to RNA-seq density)
828 change in the presence of transcriptional change, was used to detect changing TE. Numbers
829 for TE change quoted in the text refer to xtail's differential TE calls, with stepwise fold changes
830 shown in **Fig. 1**, and TE changing genes being elsewhere defined relative to E12.5
831 (**Supplementary Table 2**).
832
833 For metagene plots, a 'best transcript' (the transcript with the highest median Ribo-seq
834 coverage across all samples) was selected for each gene. These transcripts were further
835 limited to those with a length of 192 or greater. Each of these transcripts was also also
836 analyzed using the RiboDiPA [34] package, which looks for position-specific differences in Ribo-
837 seq occupancy between conditions. Since metacodon plots indicated that changes at the start
838 and stop codon were limited to a distinct region 3-4 codons from the start and stop, we divided
839 each coding sequence in to 15 bins, with 7 bins of 4 codons each centering on the start and
840 stop, and a final 'mid' bin of variable size encompassing the rest of the ORF (ORFs too short to
841 accommodate this were excluded). We then plotted bin-level log2 fold changes for each gene
842 with significant q-value of using the AUG/stop changing bins.
843
844 Fold changes were binarized into 'significant' (absolute fold change greater or less than 1.25,
845 adjusted p-value < 0.05) and 'non-significant' for plotting up and down regulated genes,
846 respectively, and GO term analysis – referred to as dTE and non-dTE in the case of TE fold-
847 change. For GO term analyses of TE change and positional Ribo-seq change, The R package
848 topGO was used.
849
850 A list of ribosomal proteins for the mouse large and small subunits were curated from Uniprot.
851
852 **tRNA abundance and codon dwell time analysis**
853 tRNA abundance was calculated from Arraystar™ Ct values by the negative delta Ct value for
854 each tRNA compared to the mean of 5S and 18S rRNA levels in each sample
855 (**Supplementary Table 4**). Abundance per-codon was calculated by taking the mean of each
856 replicate, and summing values for all relevant iso-decoders. Availability [36] was calculated as
857 the residual from a simple linear model regressing codon usage against abundance, where
858 codon usage was defined as the occurrence of that codon in the M12 coding transcriptome,

weighted by the relevant TPM of each transcript in that sample. We attempted weighting by wobble base pairs as in [41] and found this did not impact the conclusions.

We followed the approach of [35] and used RUST values as a robust estimator of codon specific dwell times. A-site occupancy was defined as the RUST value for that codon at the point of maximum variation (14 or 15 base pairs from the 5' end) with P-site occupancy defined as the RUST value 3 bp closer to the 5' from there (**Supplementary Table 4**)

Relationships between codon dwell time, tRNA abundance/availability, and amino acid identity, were investigated using the R function lm. The dataset used consisted of 269 – (i.e. one per quantified codon, per sample) with terms for the stage of the sample (S), the amino acid coded for (AA), and the abundance (or availability) of the encoding tRNAs (AB).

The largest explanatory variable was AA, which also showed a significant interaction with S, indicating that the amino acid coded for explained ~ 34% of the variance in dwell time between codons. This term also showed a significant interaction with sample stage, indicating that the amino-acid specific factors determining dwell time may vary over development (e.g., due to the availability of amino acids changing). Within a sample or across all samples, there was no association between tRNA abundance and dwell time, even after correcting for the effect of amino acid coded-for. Some codons however show a significant interaction between abundance and developmental stage, and because these codons were biased towards the high or low end of the abundance dwell time spectrum, we plotted time-relative change vs. abundance, for the top and bottom quartiles of dwell time abundance. This revealed a significant association between change in time-relative tRNA abundance and dwell time, with fastest codons showing decreasing tRNA abundance as they slowed, and the slowest codons also showing decreasing tRNA abundance.

Mass Spectrometry data processing

All raw data were analyzed and processed by MaxQuant (v1.6.0.1) [74] (**Supplementary Table 1**). Default settings were kept except that 'match between runs' was turned on. Search parameters included two missed cleavage sites, cysteine carbamidomethyl fixed modification and variable modifications including methionine oxidation, protein N-terminal acetylation and deamidation of glutamine and asparagine. The peptide mass tolerance was 6ppm and the

892 MS/MS tolerance was 20ppm. Minimal peptide length of 7 amino acids was required.
893 Database search was performed with Andromeda [75] against the UniProt/SwissProt mouse
894 database (downloaded 01/2019) with common serum contaminants and enzyme sequences.
895 The false discovery rate (FDR) was set to 1% at peptide spectrum match (PSM) level and at
896 protein level. Protein quantification across samples was performed using the label-free
897 quantification (LFQ) algorithm [76]. A minimum peptide count required for LFQ protein
898 quantification was set to two. Only proteins quantified in at least two out of the three biological
899 replicates were considered for further analyses.
900
901 To improve the match between mass spec data and sequence data, the peptides from each
902 mass spec group were matched against M12 protein sequences. Instances in which a
903 UNIPROT gene identifier did not match any gene in GENCODE, but in which the associated
904 peptide sequences matched proteins for a single GENCODE gene, were updated to match
905 that Gencode gene. All further analyses were carried out using gene-level proteomic data.
906
907 The R package proDA was used to calculate dropout-aware abundance estimates for each
908 protein group, as well as fold changes and confidence intervals relative to E12.5. For each
909 gene, a 'best' matching protein group was defined as the one with the least missing, and
910 highest median, signal across all samples, and selected for further analysis.
911
912 **Analysis of variance**
913 Analysis of variance was carried out a manner similar to [25]. We fit a linear model regressing
914 measured protein levels, or protein fold changes, P, against measured Ribo-seq or RNA-seq
915 levels R. We then performed variance decomposition using the following equation:
916

917 $$\hat{\sigma}^2_{\mathrm{PDT}} = \hat{\sigma}^2_{all} - \left(\frac{\hat{b}_{all}}{\hat{b}_R}\right)^2 \hat{\sigma}^2_R - \hat{\sigma}^2_P.$$

918 Where $\hat{\sigma}^2_{\mathrm{all}}$ represents total variance in measured protein abundance, (i.e. in proDA-normalized
919 LFQ values) and is decomposed into stochastic error in protein measurement $\hat{\sigma}^2_{\mathrm{P}}$ (estimated
920 standard error of the protein abundance model fit using proDA), systematic variation in protein
921 levels independent of R $\hat{\sigma}^2_{\mathrm{PDT}}$, and error in R measurement, where $\hat{b}_{all}$ is the linear coefficient

relating Ribo-seq and RNA-seq measurements to protein abundance, $\hat{b}_R$ is the measurement bias for R, and $\hat{\sigma}_R^2$ s the stochastic measurement error in R. Lacking a means of measuring $\hat{b}_R$ in our data, we experimented with a range of values, including the experimentally determined value of 1.21 based on NanoString measurements by [34]. We found that due to the relatively minor stochastic error in measurements of R, our estimates of $\hat{\sigma}_{\mathrm{PDT}}^2$ were robust to reasonable values of $\hat{b}_R$ (between 0.75 and 1.5) and so we elected to fix its value at 1. We then calculated variance explained as:

$$\frac{\hat{\sigma}_{\mathrm{MP}}^2 - \hat{\sigma}_P^2 - \hat{\sigma}_{\mathrm{PDT}}^2}{\hat{\sigma}_{\mathrm{MP}}^2 - \hat{\sigma}_P^2}$$

We applied this equation both within each time point, and to the fold changes between each time point. Stochastic error terms for both within-stage and between stage values for R and P were calculated using limma and proDA respectively. Notably, correlation between the two sequencing assays and MS is strongly dependent on the magnitude of change at that time point, with technical noise specific to each assay non-correlated [1]. For the R implementation of the above equations, see our github repository (https://github.com/ohlerlab/cortexomics), and the file src/Figures/Figure4/2_vardecomp.R.

Hierarchical clustering

For hierarchical clustering (**Supplementary Table 5**), we took fold changes in RNA-seq and MS values relative to E12.5, for each gene, and carried out PCA on the resulting n x 8-dimensional matrix. We calculated Euclidean distances between genes and performed hierarchical clustering using the R function *hclust* and the 'ward' clustering criterion – i.e., favoring the creation of large clusters rather than small clusters containing few outliers. We found that our expression data showed a smooth reduction in variance explained as the number of clusters varied, and so we plotted GO-term enrichment for different cluster numbers, and finding that clusters with similar GO-term enrichments began to appear at a cluster number of 13 chose this as our cutoff. Meta-trajectories for each cluster were plotted using the median and upper/lower quartiles for each cluster. Enrichment of dTE genes in each cluster

951 was calculated using Fisher's exact test (with dTE status, and inclusion in the cluster, as binary
952 variables). GO term analysis of each cluster was carried out using topGO.
953

954 **Nonlinear trajectory modeling**

955 In order to model the nonlinear relationship between steady-state protein levels and Ribo-seq,
956 a measure of protein synthesis, we used an approach similar to that used by [46] - our full
957 '*production'* model represents the expression of each protein as the result of a synthesis rate,
958 directly proportional to Ribo-seq footprint density with a proportionality constant Ks (or SDR -
959 see [38]), and a decay rate Kd:
960

961 $$\frac{d(P)}{dt} = K^s R_g(t) - K^d P(t)$$

962 If the functional form of Ribo-seq density is modeled as a linear stepwise function, this
963 equation has an analytic solution [46]. In practice, the parameters Ks and Kd will be non-
964 identifiable depending on the trajectory shape and half-life of the protein involved; for many
965 proteins, only their ratio, defining the equilibrium steady state, can be estimated (along with the
966 initial value of P). In addition to the '*production'* model, we included reduced versions of our
967 model which fixed Kd at a high value (the '*linear'* model) giving a linear protein-Ribo-seq
968 relationship, fixed Ks at a low value and modeled protein as controlled by degradation only (the
969 *'degradation'* model), or fixed both to leave protein levels stationary (the *'stationary'* model).
970 We further included a model allowing arbitrary deviations from the Ribo-seq trajectory (the
971 *'MSdev'* model), since many proteins showed changes in their trajectory that were not
972 explicable by any value of Ks and Kd. We used the bayesian information criterion (BIC) to
973 select an optimal model for each gene, further requiring that residuals in this model be
974 normally distributed (as per a chi-squared test). To estimate half-lives, we made the simplifying
975 assumption of a single Ks value applying to all genes, allowing pi-half estimates to be derived
976 for all proteins.
977

978 Stan files detailing the above models are available on the project github, and data are in
979 **Supplementary Table 5**.
980

981 **Single cell RNA-seq data**

982 Single cell RNA-seq (scRNA-seq) data was derived from data and scripts in [4] and
983 accompanying web resource:
984 http://genebrowser.unige.ch/telagirdon/#query_the_atlas.
985
986 For each gene, it's occurrence in neocortex cells measured by scRNA-seq is presented as a
987 heat map arranged by chronological time of cell collection (x-axis) vs. time since cell birth (y-
988 axis), after a timed pulse with a FlashTag label *in utero*. These axes correspond to roughly
989 orthogonal programs of gene expression change, with the y-axis describing differences
990 between apical progenitors and differentiated neurons, and the x-axis describing differences
991 between cells born at different stages of development.
992

993 **Sequence motif analysis**

994 Motif analysis was performed with the AME program from the Meme suite as per [46,77] because
995 we observed a systematic difference in UTR length between TE changing and TE unchanging
996 genes. AME requires that input and control sequences are of approximately equal length
997 distribution, so we created a sample of TE changing genes whose length distribution matched
998 that of the TE unchanging genes. We ran AME with the CISBP-RNA database of RNA-binding
999 protein motifs [78].
1000

1001 **Immuno-electron microscopy**

1002 Fixation, sectioning, immunolabeling, and electron microscopy were performed as described
1003 previously [15]. E12.5 and E15.5 neocortex coronal sections were labeled with mouse anti-Rps5
1004 (uS7; Santa Cruz, sc-390935) followed by 2.5 nm nanogold conjugated secondary antibody
1005 (Nanoprobes, 2001). Imaging was performed at 2700 x magnification on a Tecnai Spirit
1006 electron microscope. Quantification was performed in FIJI [79] with the Process > Find Maxima
1007 tool, and Measure > Area tool, followed by statistical analysis in GraphPad Prism (GraphPad
1008 Software Inc.) to calculate puncta per μm^2 (Welch's ANOVA, Dunnett's *post hoc* test)
1009 (**Supplementary Table 3**). Primary antibody leave-out controls were prepared in parallel, and
1010 were absent of nanogold signal.
1011

1012 **Expression vectors**

1013 For tdTomato reporter experiments, we used beta-actin driven expression constructs *pCAG-*
1014 *EGFP* and *pCAG-flox-STOP-flox-tdTomato*, as described previously [31]. A control vector with

1015 scrambled non-silencing shRNA [59] was obtained from Thermo Scientific, and the shRNA to
1016 knock-down plasmid for mouse *eIF4EBP1* was obtained from Sigma Aldrich
1017 (TRCN0000335381).
1018

1019 ***In utero* electroporation (IUE)**

1020 Mouse embryos were subjected to IUE exactly as described previously [31,59,80]. For the
1021 experiments with the tdTomato reporter in the Satb2$^{Cre/+}$ line, we used an equal amount of
1022 *pCAG-GFP* and *pCAG-flox-stop-flox-tdTomato*.
1023

1024 **Fluorescent *in situ* hybridization (FISH)**

1025 *In situ* hybridization using RNAscope Technology to detect mRNA of *m. musculus Satb2*
1026 (413261) and *Bcl11b* (413271-C2) was performed according to the manufacturer's protocols
1027 (ACD, 323100). Prior to hybridization, embryonic brains at E12.5, E14.5 and E16.5 were
1028 collected in PBS, fixed in 4 % PFA/PBS prepared with DEPC for 16-20 hours at 4 °C. Brains
1029 were then incubated in sucrose solutions (10 % - 20 % - 30 %/PBS) until they reach osmotic
1030 equilibrium, embedded in O. C. T. Compound (Tissue-Tek) in a plastic cryoblock mold and
1031 frozen on dry ice. Coronal sections of 16 µm thickness were collected using a cryostat.
1032

1033 **Cryosectioning**

1034 For all histological procedures, brain sections were prepared on a Leica CM3050S cryostat.
1035 Prior to cryosectioning, brains were incubated for at least 5 hours with 10% sucrose in PBS,
1036 followed by incubation with 30% sucrose in PBS until the tissue reached osmotic equilibrium.
1037 Next, brains were frozen in -38 to -40°C isopentane (Roth). For processing of the tissue after *in*
1038 *utero* electroporation, coronal cryosections of 50 µm thickness were collected in PBS/0.01%
1039 sodium azide solution. For *in situ* hybridization and the mRNA/protein colocalization
1040 experiments, 16 µm sections were collected.
1041

1042 **Immunohistochemistry**

1043 Fixed brain sections were washed with PBS three times at room temperature prior to the
1044 procedure to remove the sucrose and freezing compound residue. The sections were then
1045 incubated with Blocking solution (5% goat serum, 0.5% (v/v) Triton X-100, PBS) for one hour
1046 at room temperature, then with the primary antibody and DAPI diluted in blocking buffer for 16-
1047 20 hours at 4 °C, washed in PBS three times for 30 minutes and incubated with secondary

antibody diluted in the blocking buffer for up to four hours at room temperature. Next, sections were incubated with PBS for 30 minutes three times and mounted with a cover glass (Menzel-Gläser) and Immu-Mount mounting medium (Shandon, Thermo-Scientific). For experiments with dual mRNA and protein labeling, instead of mounting after the hybridization protocol, the sections were subjected to the immunohistochemistry as described here.

Antibodies for immunohistochemistry

Primary antibodies used for immunocytochemistry were used at dilutions indicated: anti-Satb2 (1:500, rabbit, home-made; [31]), anti-Bcl11b (1:500, rat, Abcam, 25B6, anti-Ctip2, RRID:AB_2064130), anti-GFP (1:1000, goat, Rockland, RRID:AB_2612804), anti-Cre (1:1000, rabbit, SySy, RRID:AB_2619968), anti-Tbr2 (1:300, rabbit, Abcam, RRID:AB_778267), anti-Pax6 (1:500, rabbit, Millipore, RRID:AB_1587367), Draq5 (1:2000), anti-eIF4EBP1 (1:1000, rabbit, Abcam, ab32024, RRID:AB_2097990. All secondary antibodies were from Jackson Immunoresearch and were used at 1:250.

Confocal imaging

Imaging of brain coronal cross sections after IUE was performed at the level of primary somatosensory cortex primordium. For imaging of the overview of immunostaining, a Leica SPL confocal microscope with 20X, 40X and 63X objectives was used. For quantitative imaging of FISH signal, a Leica Sp8 microscope with 40X objective was used. Quantification of mRNA cluster sizes, and mRNA and protein localization, was performed using ImageJ software.

Quantification of distribution and size of mRNA clusters

mRNA puncta were quantified using ImageJ software. The maximum intensity of confocal image Z-stacks was projected on a single 2D plane. After thresholding, the images were binarized using the watershed segmentation to separate cluster clouds. The number of particles of 0.1 μm^2 or bigger were then quantified using Measure Particles tool and normalized to the number of DAPI-labeled nuclei in a given cortical area (VZ, CP, etc.). Area of clusters was quantified as well and expressed as an absolute surface. See **Supplementary Table 3.**

Quantification of colocalization

1081 Mander's colocalization coefficient was quantified for neurons expressing Satb2 and Bcl11b
1082 protein and mRNA. Protein colocalization was determined manually, and RNA colocalization
1083 was quantified using binarized images after multiplication. See **Supplementary Table 3.**
1084

1085 **Quantification of neuronal cell markers**

1086 The manually quantified number of neurons expressing a given marker was normalized to the
1087 entire number of IUE-labeled neurons or to DAPI-labeled nuclei count. See **Supplementary**
1088 **Table 3.**
1089

1090 **Statistical analyses**

1091 Statistics were performed using SPSS v.17 (San Diego, USA) or GraphPad Prism software. All
1092 numerical values and description of statistical tests used, definition of center, dispersion,
1093 precision, and definition of significance can be found in **Supplementary Table 3**. Prior to
1094 comparison of experimental groups, normality and log-normality test were performed.
1095

1096 **Data availability**

1097 Code generated during this study is supplied at: https://github.com/ohlerlab/cortexomics.
1098 Further requests may be directed to and will be fulfilled by the Lead Contact,
1099 matthew.kraushar@molgen.mpg.de (M.L.K.). Data have been deposited in publicly available
1100 repositories as indicated:
1101 RNA-seq data are publicly available in the NIH GEO: GSE157425.
1102 Ribo-seq data are deposited in the NIH GEO: GSE169457.
1103 tRNA qPCR array data are deposited in the NIH GEO: GSE169621.
1104 Mass spectrometry data are publicly available in the ProteomeXchange: PXD014841.

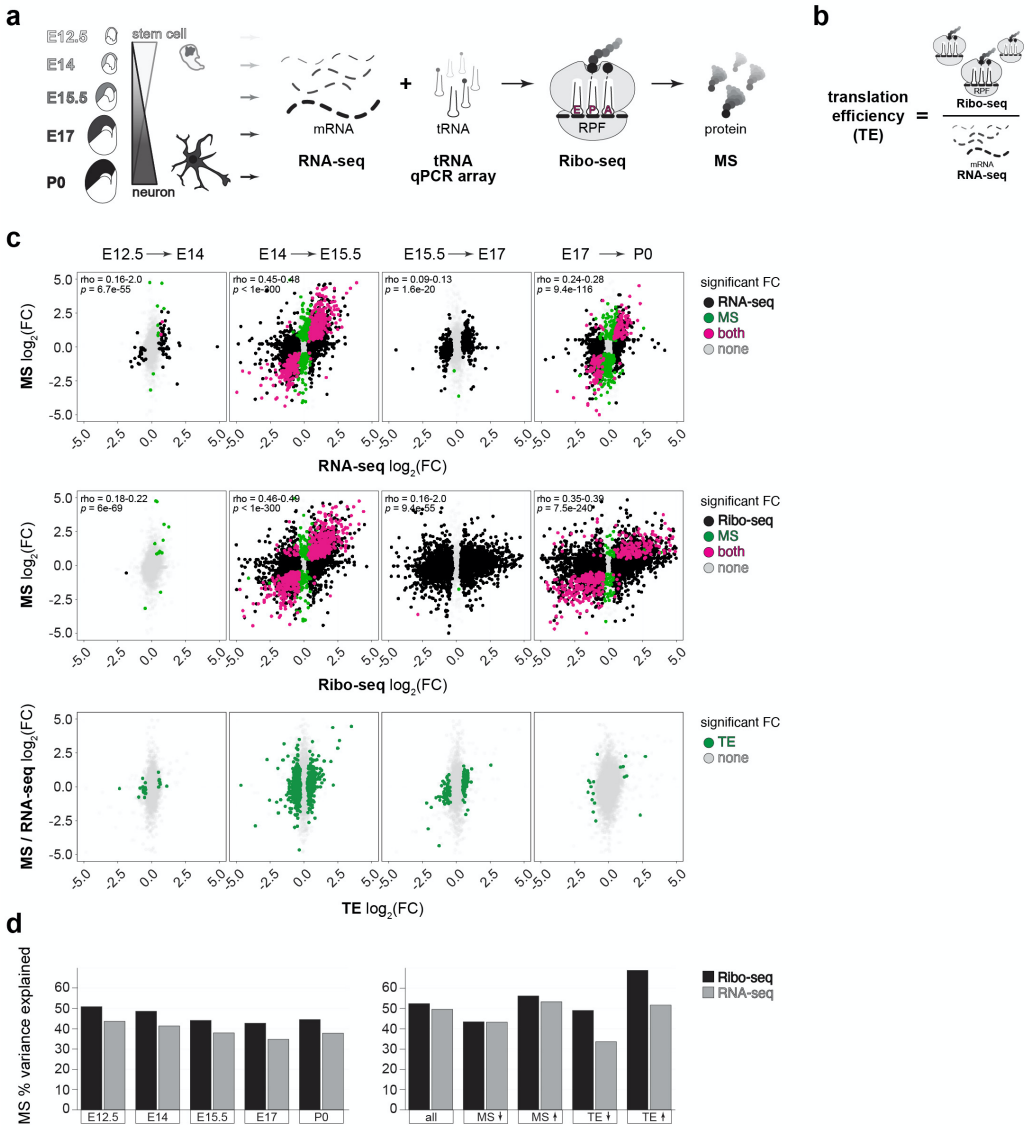

Fig. 1. A transient spike in translation regulation occurs at mid-neurogenesis during prenatal development. **a**, Neural stem cell differentiation in the brain's neocortex, analyzed by RNA-seq, Ribo-seq, tRNA qPCR array, and MS at embryonic (E12.5-E17) and postnatal (P0) stages. **b**, Schematic of translation efficiency (TE). **c**, Sequential fold changes in post-transcriptional gene expression between adjacent stages, comparing mRNA vs. protein (top), mRNA translation vs. protein (middle), and calculated translation efficiency (bottom). Significance assessed at ≥ 1.25 FC, $p < 0.05$. **d**, The percent variance in MS explained by RNA-seq or Ribo-seq at each developmental stage, and for subgroups with MS and translation efficiency changes. See also **Extended Data Figs. 1-2** and **Supplementary Tables 1-2**.

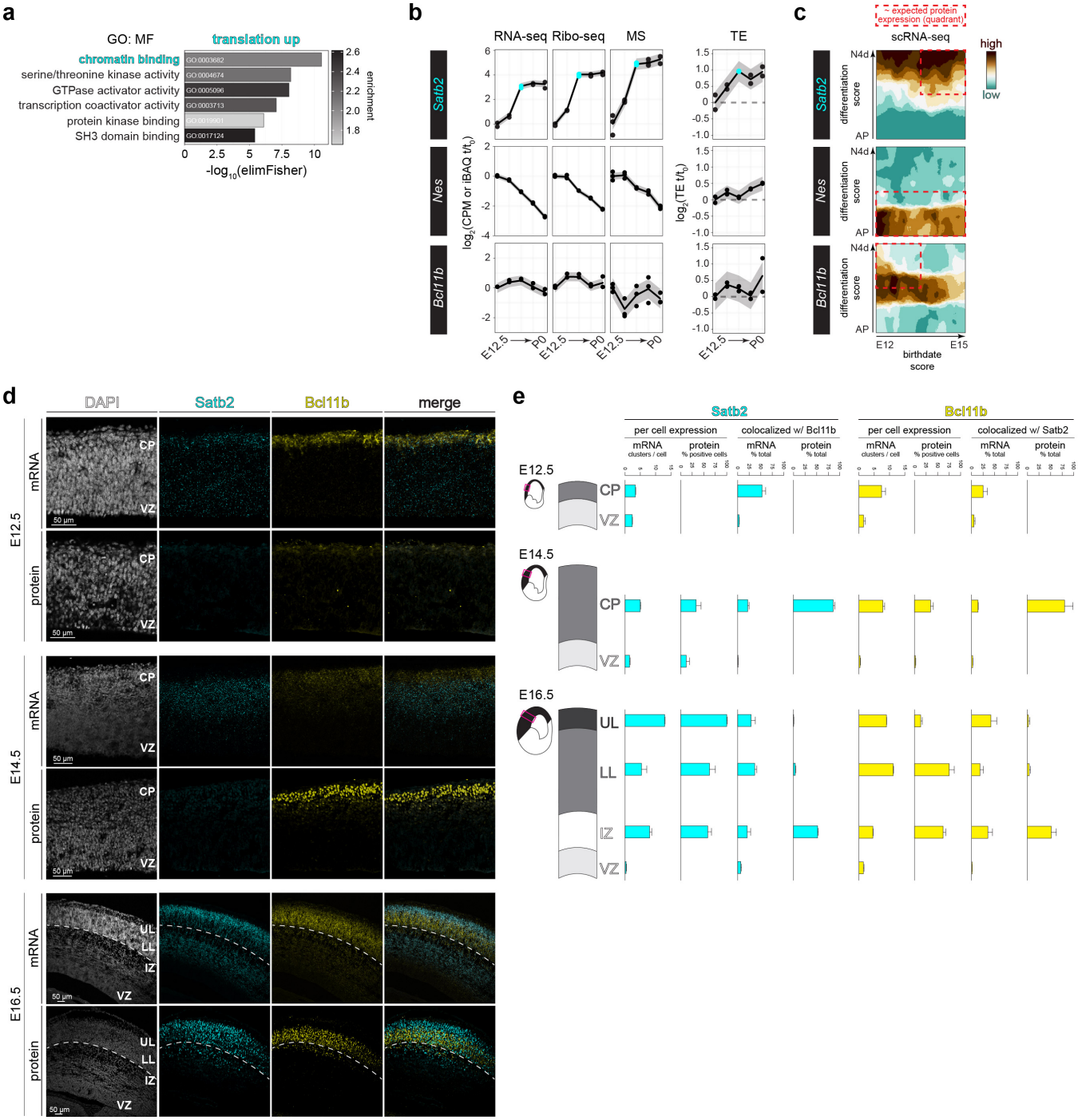

Fig. 2. Translation upregulation of *Satb2* leads to divergent spatiotemporal mRNA and protein expression. **a**, Gene ontology (GO, molecular function) analysis of translationally up-regulated (TE up) mRNAs. **b**, The median trajectory of *Satb2, Nes,* and *Bcl11b* gene expression measured by RNA-seq, Ribo-seq, MS, and translation efficiency. The E15.5 timepoint is highlighted for Satb2 **c**, *Satb2, Nes,* and *Bcl11b* expression in scRNA-seq data tracking differentiating neocortex cells at 1, 24, or 96 hours after birth (y-axis), at birthdates E12, E13, E14, or E15 (x-axis) (Telley et al., 2019). Expected distribution of protein expression (DeBoer et al., 2013) is outlined. **d**, Neocortex coronal sections at E12.5, E14.5, and E16.5 analyzed for *Satb2* and *Bcl11b* mRNA by fluorescence *in situ* hybridization, and protein by immunohistochemistry. Deep border of the cortical plate is demarcated at E16.5 (dotted line). DAPI (nuclei). Ventricular zone (VZ), cortical plate (CP), lower layers (LL), upper layers (UL). **e**, Quantification of (d). Mean ± SEM. See also **Extended Data Fig. 3a-b** and **Supplementary Table 3**.

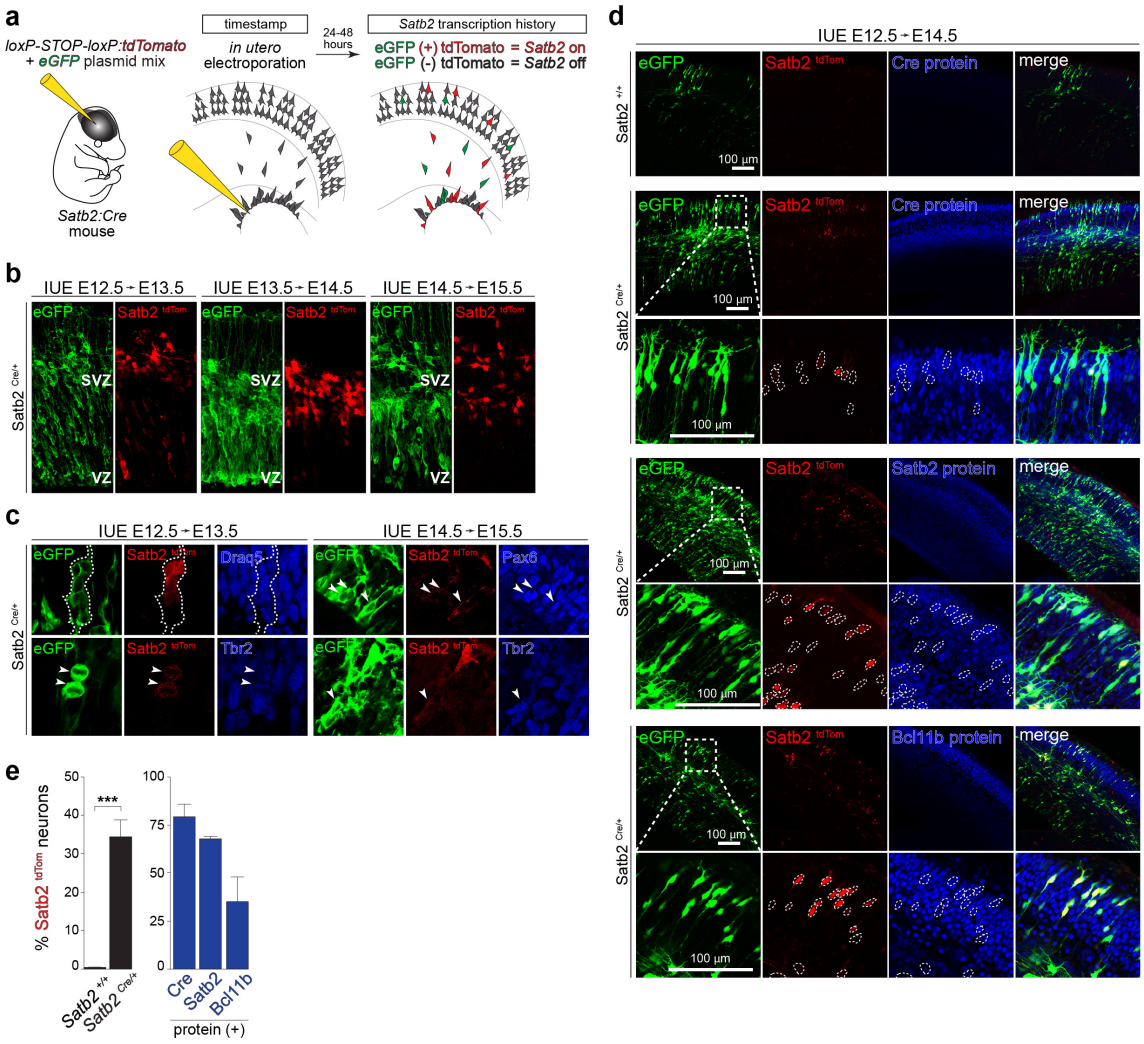

Fig. 3. *Satb2* transcription is broad across neuronal lineages with more restricted translation.
a, Schematic of the experimental approach. **b**, *Satb2* transcription activity visualized by Cre-driven (*Satb2*$^{Cre/+}$) tdTomato expression, with reporter *in utero* electroporation (IUE) at E12.5, E13.5, or E14.5 and imaged after 24 hours. Co-electroporation of an eGFP plasmid labels all transfected cells. Ventricular zone (VZ), subventricular zone (SVZ). **c**, *Satb2*^{tdTom} co-immunolabeling with Pax6 (apical progenitors), Tbr2 (intermediate progenitors), and Draq5 (nuclei). **d**, *Satb2*^{tdTom} expression at E12.5-E14.5, with co-immunolabeling for neuronal fate determinant proteins Satb2 and Bcl11b, among all electroporated cells (eGFP). Negative control is the absence of *Cre* (Satb2$^{+/+}$). **e**, Quantification of (d) for the expression of Cre, Satb2, and Bcl11b proteins in cells transcribing *Satb2* mRNA (*Satb2*^{tdTom}). Mean ± SD, unpaired t-test, ***$p < 0.0001$. See also **Extended Data Fig. 3c** and **Supplementary Table 3**.

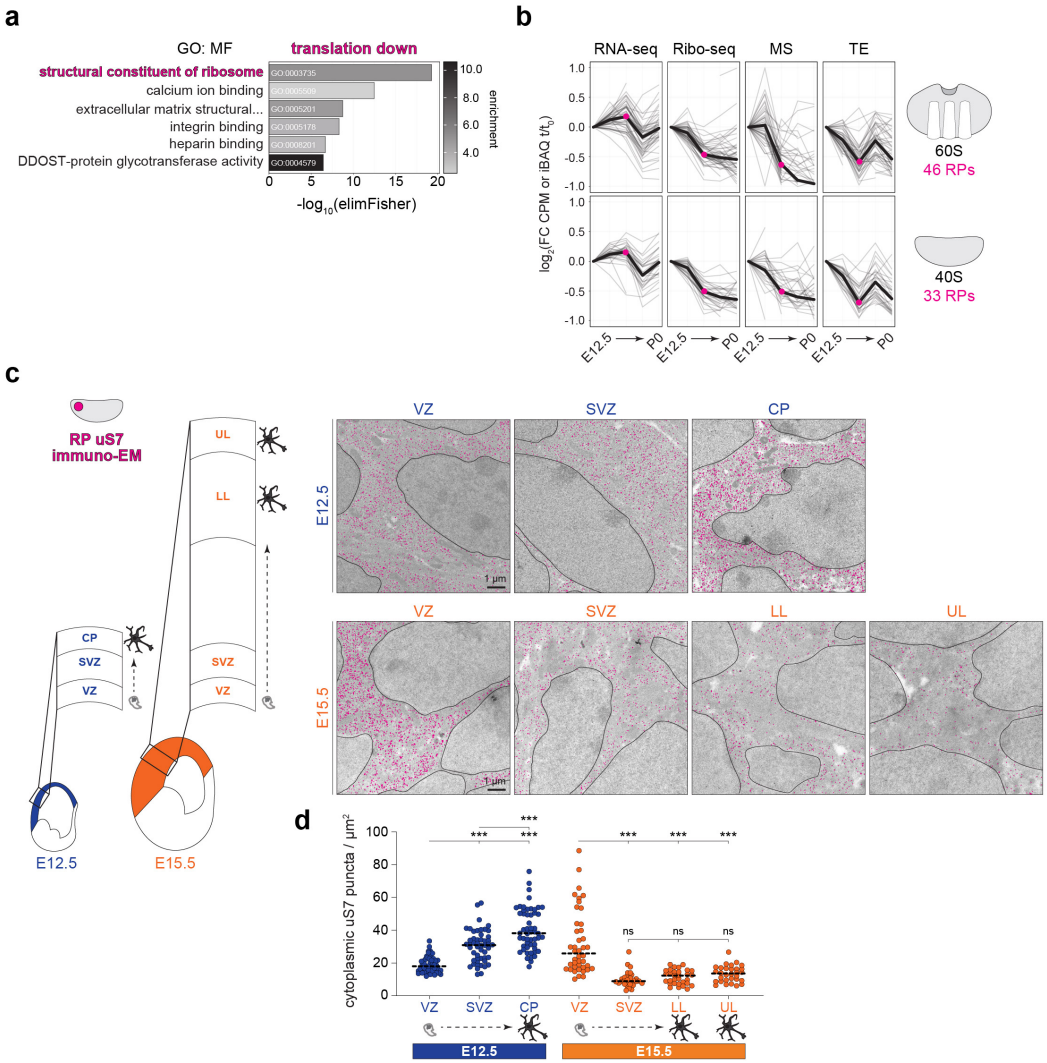

Fig. 4. Translation downregulation decreases ribosome levels acutely at mid-neurogenesis.
a, Gene ontology (GO, molecular function) analysis of translationally down-regulated (TE down) mRNAs. **b**, The expression trajectories (grey) of all 79 ribosomal protein coding mRNAs in the large (*Rpl*) and small (*Rps*) subunits from E12.5 (t_0) to subsequent stages (t), measured by RNA-seq, Ribo-seq, MS, and calculated translation efficiency. Median trajectories are shown (black). **c**, Immuno-electron microscopy labeling ribosomal protein uS7 (magenta) in the E12.5 and E15.5 neocortex neural stem cells and neurons, with **d**, quantification for ribosomes per cytoplasmic area. Mean shown (line), Welch's ANOVA and Dunnett's *post hoc* test, ***$p < 0.001$. Neural stem cells are located in the ventricular zone (VZ) and sub-ventricular zone (SVZ); post-mitotic neurons are located in the cortical plate (CP), lower layers (LL), upper layers (UL). Nuclei are outlined. See also **Extended Data Fig. 4** and **Supplementary Table 3**.

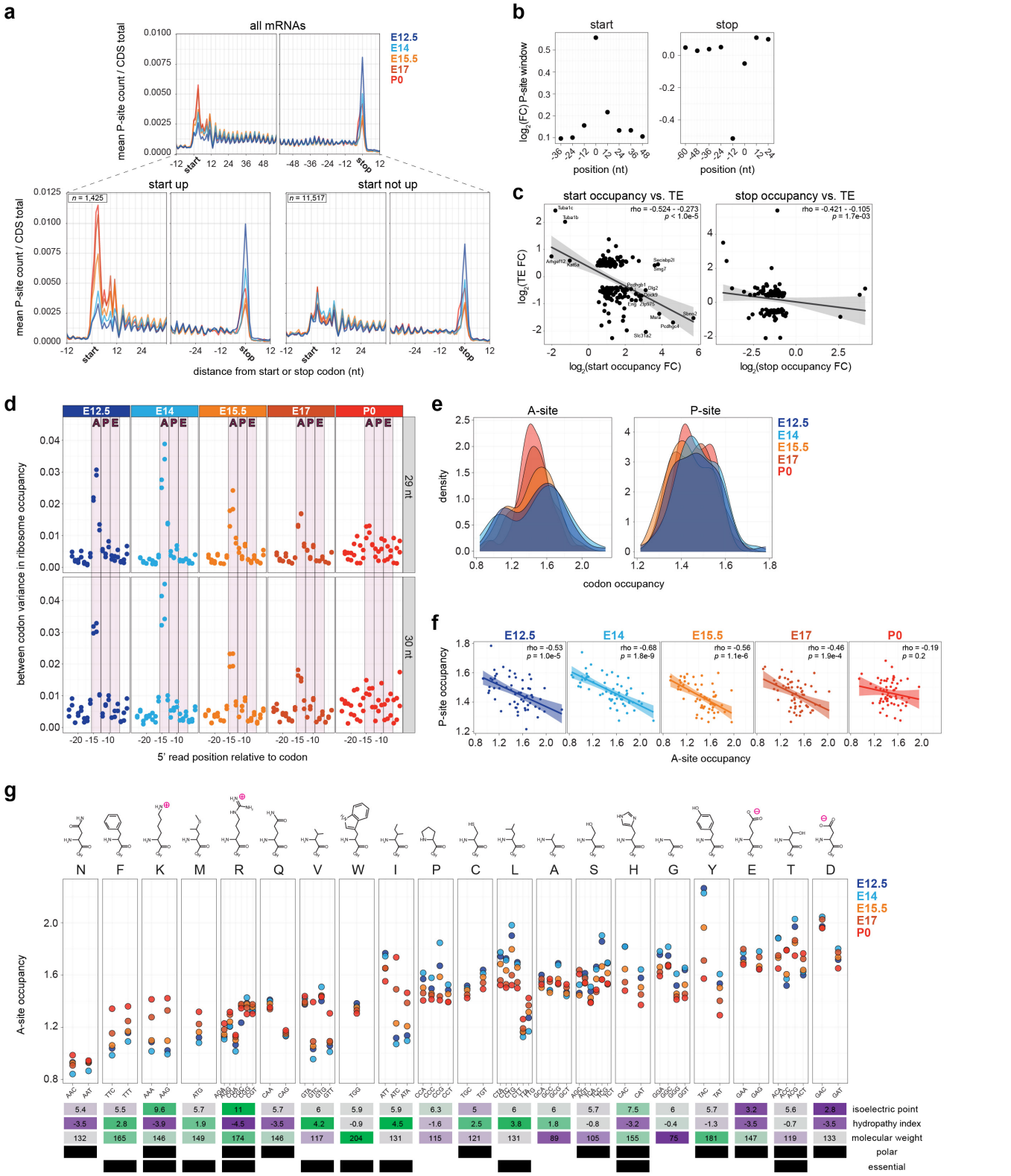

Fig. 5. Ribosome density at the start codon and in the CDS shifts sharply at mid-neurogenesis.
a, Ribosome occupancy metagene plot including all mRNAs (top) surrounding the start (left) and stop (right) codons at five stages. Separation of mRNAs by changing or unchanged start codon occupancy (bottom). **b**, Position specific fold changes in ribosome P-site counts surrounding the start and stop codons. **c**, Start (left) and stop (right) codon occupancy vs. TE fold change per gene. **d**, Between codon variance in ribosome occupancy of A-, P-, and E-sites at each stage. Calculation with both 29 nt (top) and 30 nt (bottom) RPF fragments shown. **e**, Distribution of per-codon A- and P-site occupancy at each stage. **f**, Correlation between A- and P-site occupancy per codon. **g**, Ribosome A-site occupancy for each amino acid with corresponding synonymous codons at each stage. See also **Extended Data Figs. 5-6**, **Supplementary Table 4**.

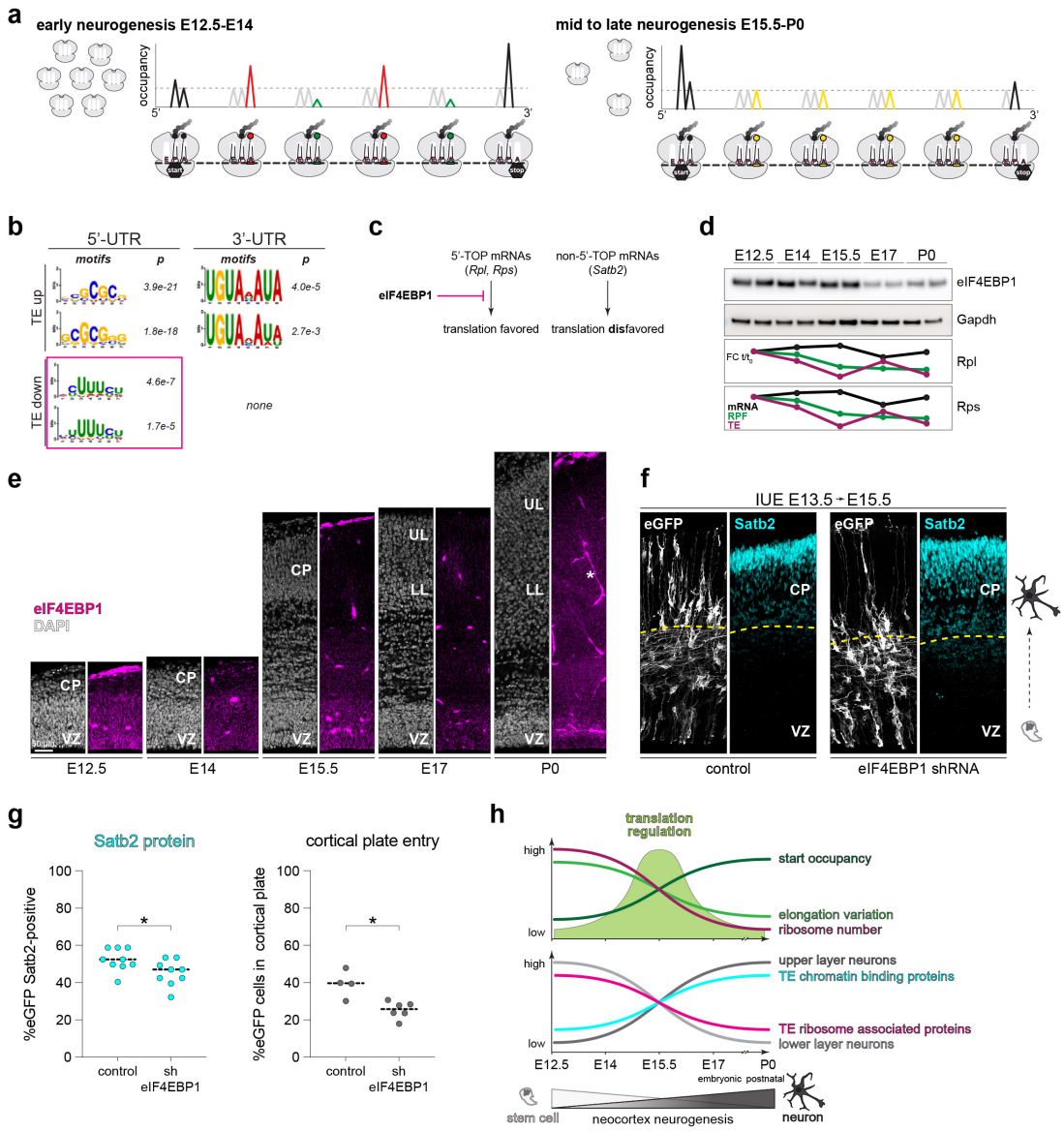

Fig. 6. eIF4EBP1 levels coincide with ribosome abundance and control neuronal Satb2 fate *in vivo*.
a, Model of early vs. late neurogenesis ribosome levels and per-codon changes in ribosome occupancy. **b**, Positional weight matrix of the top two motifs ranked by *p*-value in the 5' and 3'-UTRs of TE up or down mRNAs. 5' terminal oligopyrimidine (TOP) motifs are highlighted for TE down genes. **c**, eIF4EBP1 inhibition of ribosomal protein coding mRNA 5'-TOP sequence translation. **d**, Western blot analysis of eIF4EBP1 levels in neocortex lysates in biological duplicate (n = 4-6 neocortex hemispheres per lane). Concurrent trajectory of Rpl and Rps translation shown below. **e**, Immunohistochemistry analysis of eIF4EBP1 expression in neocortex coronal sections across neurogenesis. Blood vessels (star) are a common staining artifact. **f**, shRNA knockdown of eIF4EBP1 compared to scrambled control by *in utero* electroporation (IUE) at E13.5 followed by analysis at E15.5 with Satb2 protein immunolabeling. Co-electroporation of eGFP labels all transfected cells. Cortical plate neuron boundary is demarcated (dotted line). **g**, Quantification of (f) per animal for the percent of electroporated cells expressing Satb2 protein (left), and number of cells migrating into the cortical plate (right). Median (line), Mann-Whitney test, *p < 0.05. **h**, Summary of timed translation changes and neuronal specification during neocortex development. See also **Supplementary Table 3**.

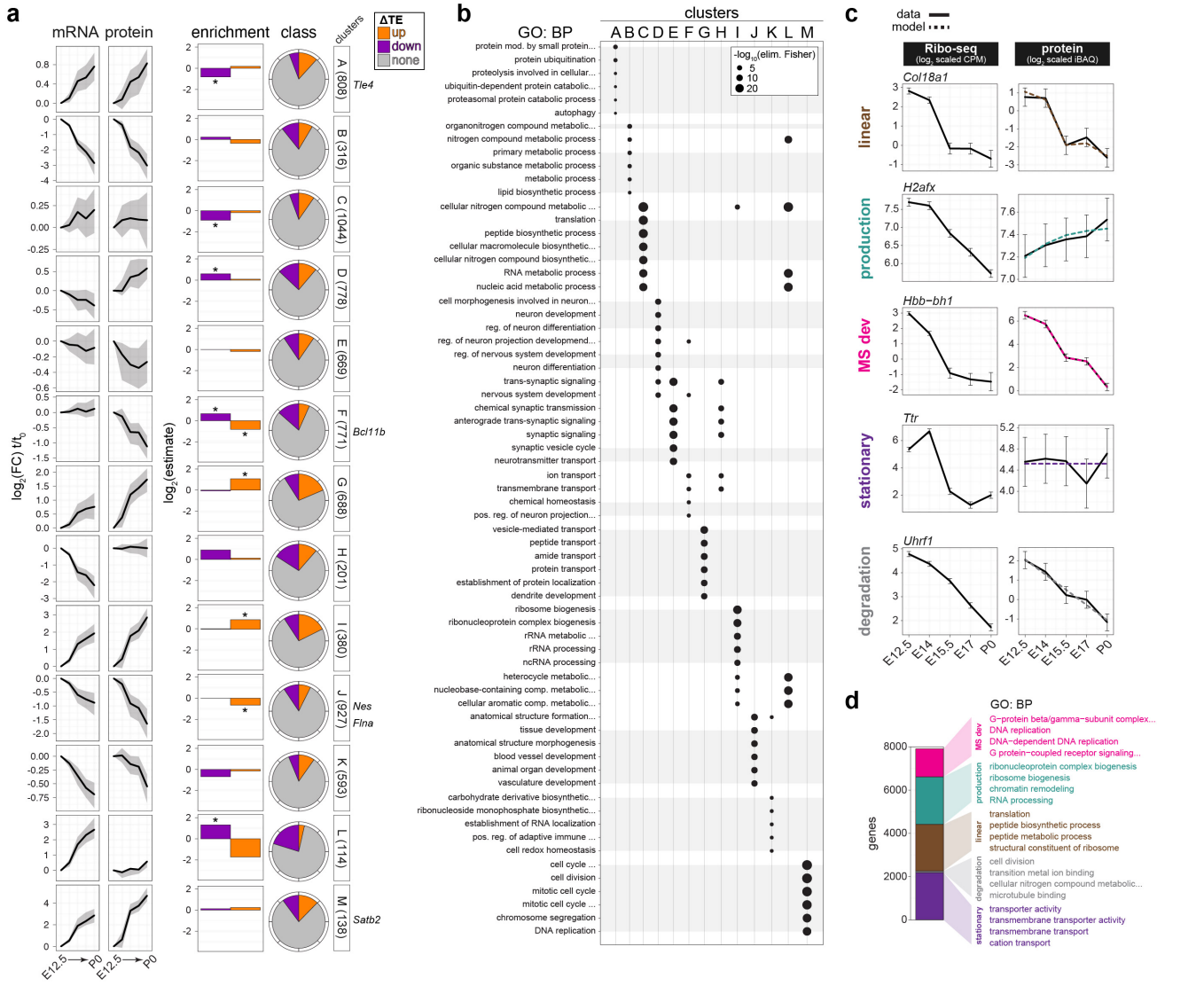

Fig. 7. Modeling divergent trajectories of mRNA and protein expression by translation regulation.
a, mRNA (RNA-seq) and protein (MS) expression per gene from E12.5 (t_0) to subsequent stages (t) clustered by trajectory. The median trajectory is shown, with upper and lower quartiles (grey). Enrichment and proportion of TE up and down genes in each cluster, with significant enrichment (*p < 0.05). Example neural stem cell and neuronal marker genes are indicated (right). **b**, Gene ontology (GO, biological process) enrichment for each cluster, with unique terms for a cluster outlined in grey. **c**, Modeling of non-linear relationships between Ribo-seq and MS comparing active translation vs. steady-state protein, with representative genes shown for each category. See text for details. **d**, Proportion of total genes in each category from (c), with enriched GO terms per category. Fisher's exact test, p < 0.05. See also **Extended Data Fig. 7**, **Supplementary Table 5**, and https://shiny.mdc-berlin.de/cortexomics/.

Extended Data

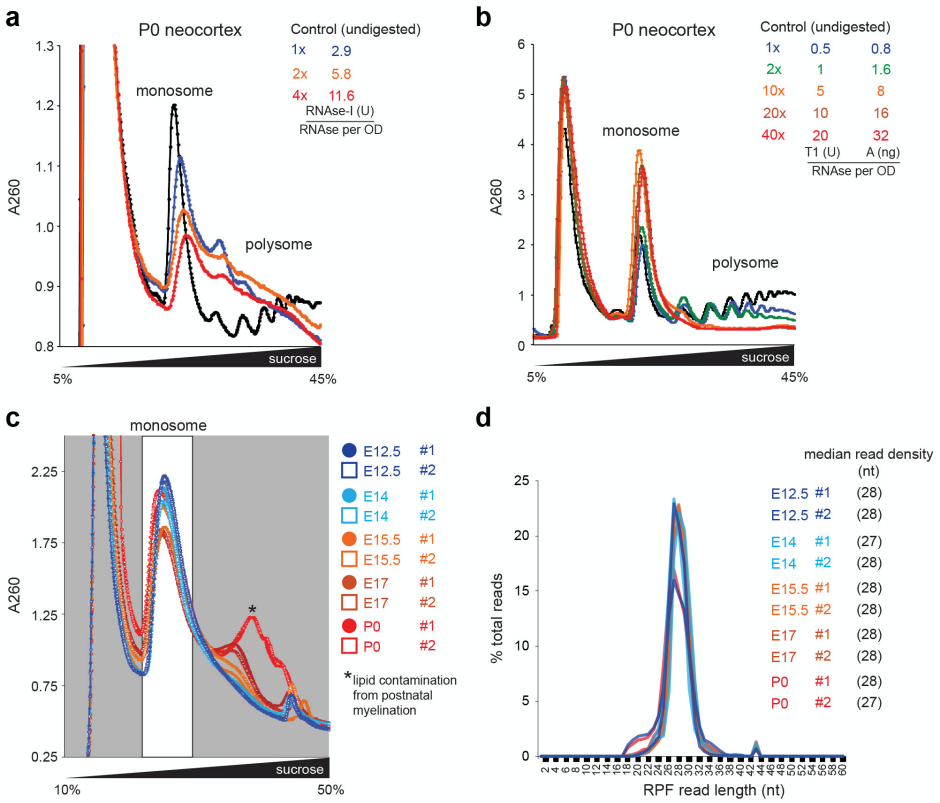

Extended Data Fig. 1. Optimized ribosome protected mRNA fragment purification from neocortex.
Nuclease digestion for the generation of ribosome protected mRNA fragments (RPFs) from P0 neocortex, with **a**, RNAse-I vs. **b**, a combination of RNAse-T1 & A. Absorbance at 260 nm (A260). Chains of actively translating ribosomes (polysome) should be digested into single ribosomes (monosome). RNAse-I, typically used in yeast, was inefficient in neocortex lysates, and thus an RNAse-T1 & A protocol was used for this study. **c**, Nuclease digestion and purification of neocortex RPFs in biological duplicates at each developmental stage with the optimized protocol from (b). Each biological replicate included 17-40 brains (34-80 neocortex hemispheres) as detailed in the **Methods**. **d**, RPF read length distribution. Associated with **Fig. 1**. See also **Supplementary Table 1**.

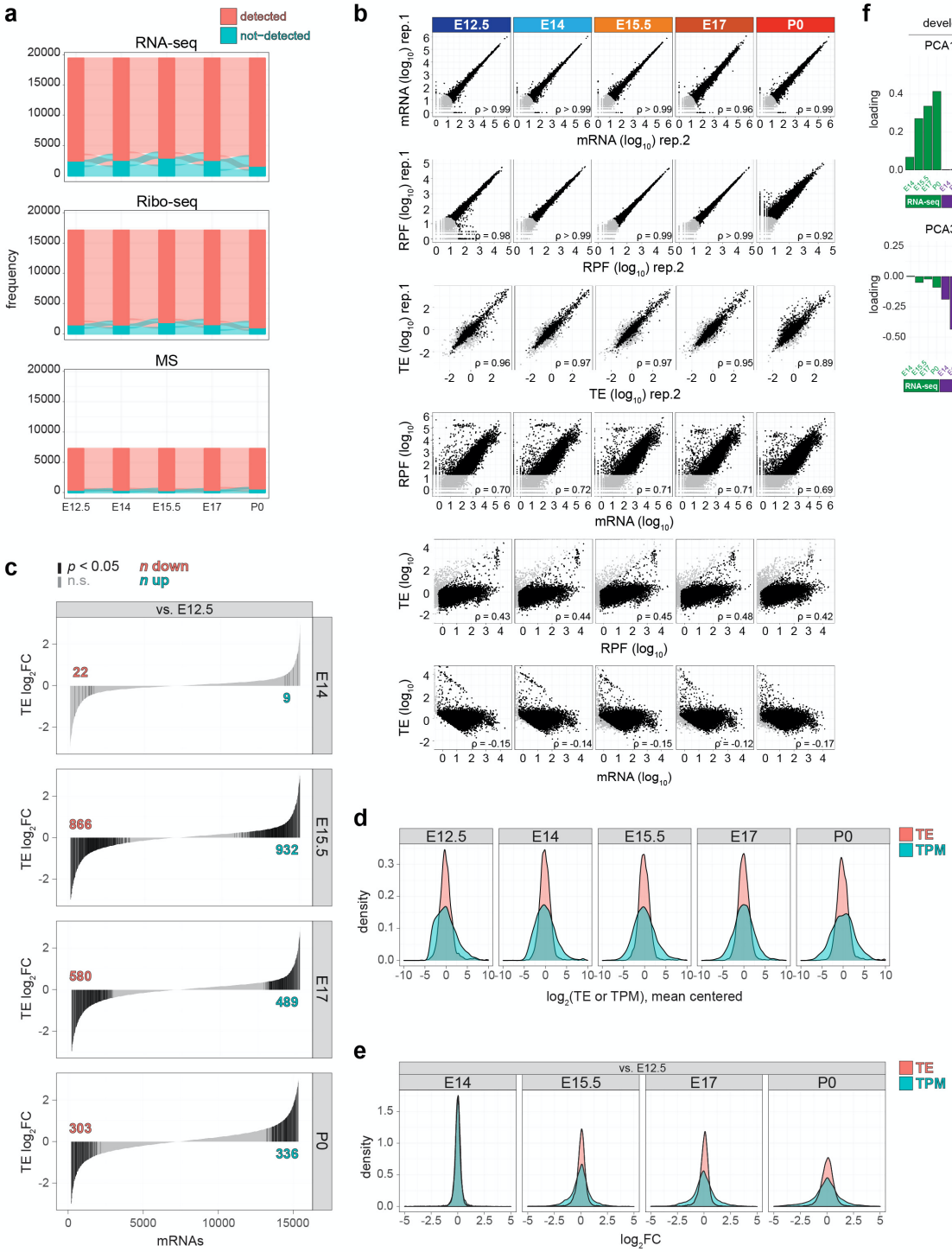

Extended Data Fig. 2. Neocortex RNA-seq, Ribo-seq, MS, and translation efficiency data characteristics. **a**, River plots demonstrating the number of unique genes detected across all 5 stages measured by RNA-seq, Ribo-seq, or mass spectrometry, compared to the number detected in <5 stages. **b**, Biological replicates of transcripts per million (TPM) measured by RNA-seq (mRNA), Ribo-seq (RPF), and calculated translation efficiency (TE), including correlations between RPF and TE with mRNA to highlight genes with robust translation regulation. **c**, The distribution of TE up and down fold changes (FC) compared to the earliest stage E12.5, with significant genes highlighted in black ($p < 0.05$). **d**, The distribution of TE and mRNA abundance (TPM) for all genes at each stage, and **e**, fold changes vs. the earliest stage E12.5. **f**, Principal component analysis (PCA) of developmental fold changes in RNA-seq, TE, and MS compared to the earliest stage E12.5. The first four components are shown, with percent variance annotated. Associated with **Fig. 1**. See also **Supplementary Tables 1-2**.

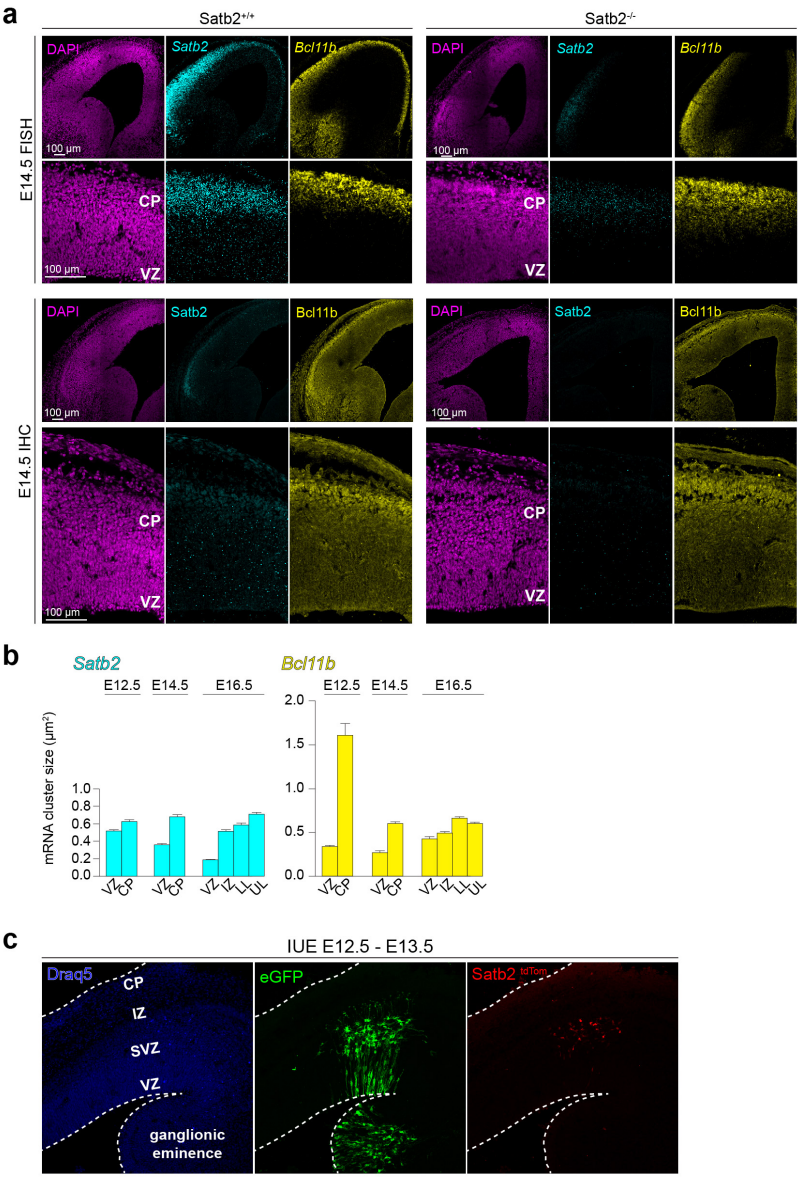

Extended Data Fig. 3. *Satb2*$^{-/-}$ control for FISH and IHC and neocortex-specific *Satb2* transcription.
a, Fluorescence *in situ* hybridization (FISH) and immunohistochemistry (IHC) probing for *Satb2* and *Bcl11b* mRNA and protein, respectively, in wild-type (*Satb2*$^{+/+}$) and *Satb2* knockout (*Satb2*$^{-/-}$) neocortex coronal sections at E14.5. Ventricular zone (VZ), cortical plate (CP). **b**, Measurement of *Satb2* and *Bcl11b* mRNA cluster sizes in FISH probed neocortex sections at three developmental stages. Intermediate zone (IZ), lower layers (LL), upper layers (UL). Mean ± SEM. **c**, *Satb2* transcription activation visualized in *Satb2*$^{Cre/+}$ mice by *in utero* co-electroporation of the neocortex and ganglionic eminence with a *loxP-STOP-loxP-tdTomato* (*Satb2*^{tdTom}) fluorescence reporter at E12.5, along with eGFP reporter for all transfected cells, and analysis in coronal sections at E13.5. Sub-ventricular zone (SVZ). Associated with **Figs. 2-3**. See also **Supplementary Table 3**.

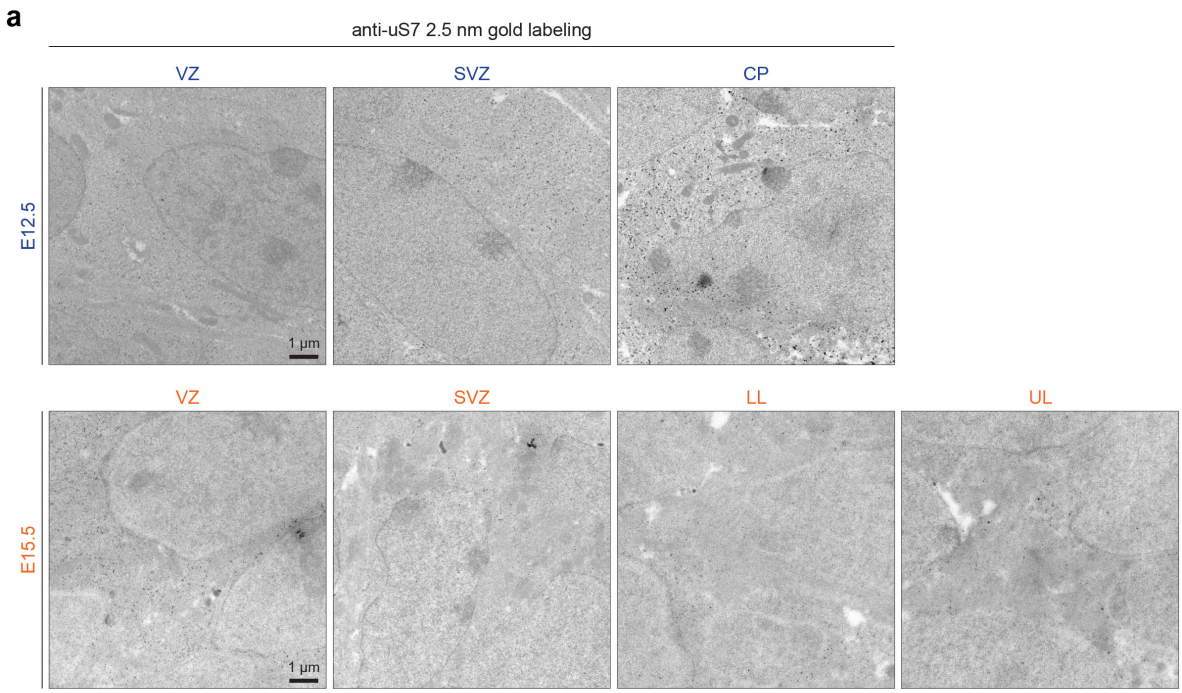

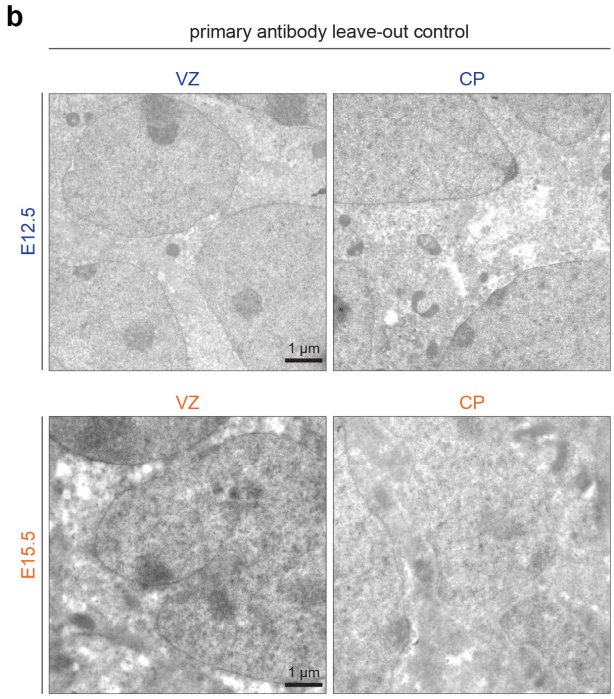

Extended Data Fig. 4. Immuno-electron microscopy labeling of ribosomes.
a, Raw images of neocortex coronal sections at E12.5 and E15.5 shown in **Fig. 4c**, immunolabeled with anti-ribosomal protein uS7 followed by 2.5 nm gold secondary (dark black spots), which were automatically detected and quantified in FIJI (magenta spots in **Fig. 4c**). Electron microscopy was performed in regions corresponding to the stem cell niches of the ventricular zone (VZ) and sub-ventricular zone (SVZ), in addition to regions of differentiating neurons in the cortical plate (CP), which includes both lower layers (LL) and upper layers (UL) at later stages. Quantification of nanogold secondary signal was performed per unit area of the cytoplasm, with nuclei excluded by tracing the nuclear membrane (black lines in **Fig. 4c**). **b**, Primary antibody leave-out controls were prepared in parallel.

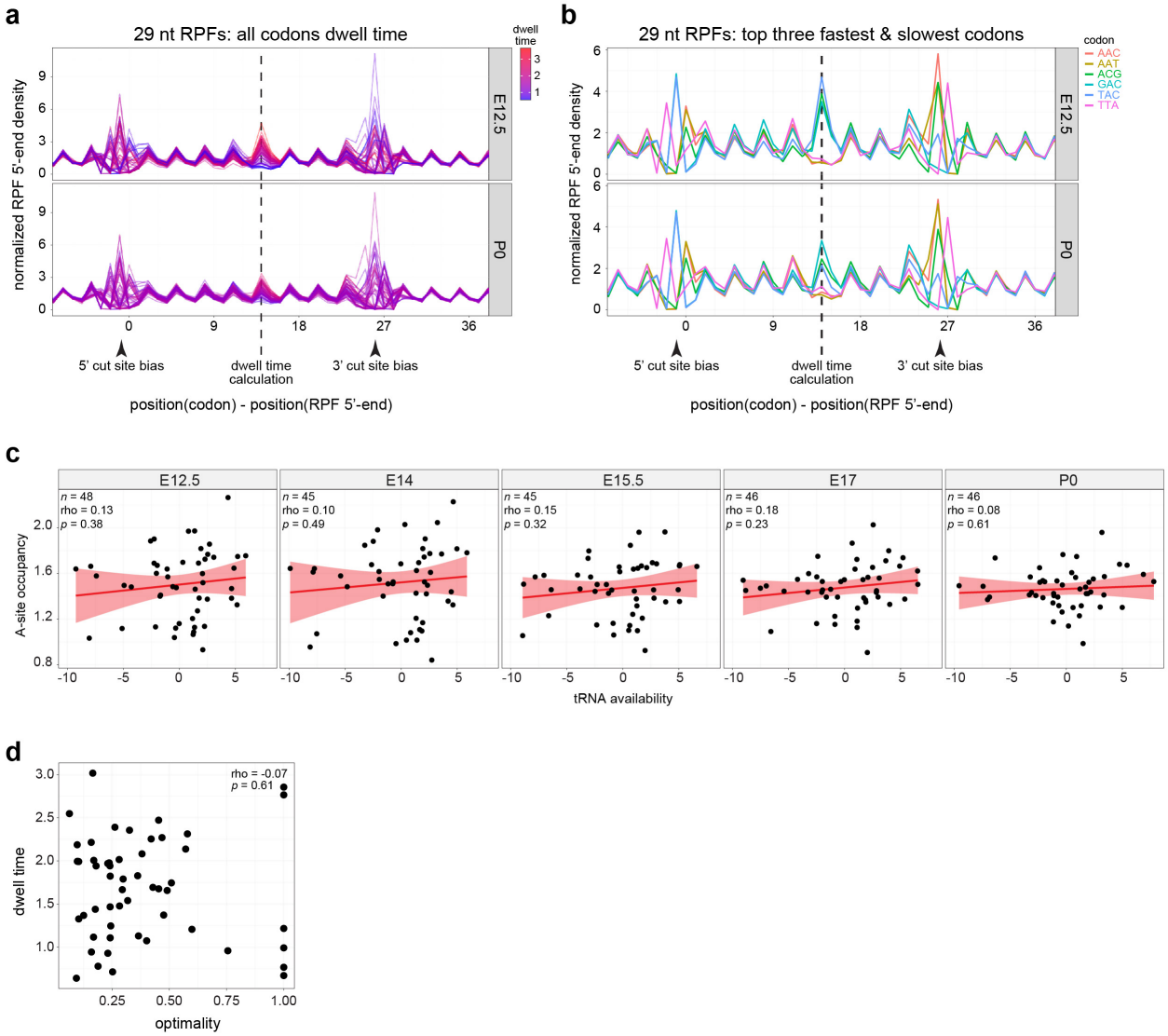

Extended Data Fig. 5. Analysis of per-codon ribosome density.
5' normalized ribosome-protected mRNA fragment (RPF) density for **a**, all codons and **b**, the top 3 slowest/fastest codons. Plotting the normalized density of Ribo-seq read 5' ends relative to each codon/read length/sample shows two strongly variable regions corresponding to 5'- and 3'-end cut site biases during nuclease digestion. A third variable region in between corresponds to RPFs with their A/P-sites positioned over the codon. We infer the location of the A-site as the 3 bp region showing the most inter-codon variability, and use the normalized occupancy here to measure codon dwell times, and variance between codons. Independently, this region also identifies the location of intra-codon variability between samples. **c**, Per-codon correlation between tRNA availability calculated from tRNA qPCR array (see **Methods**), and the ribosome occupancy of that codon when positioned in the A- or P-site of the ribosome footprint. **d**, Correlation between ribosome dwell time per codon and the optimality of the codon as defined in (dos Reis et al., 2004), with the mean across all stages shown. Associated with **Fig. 5**. See also **Supplementary Table 4**.

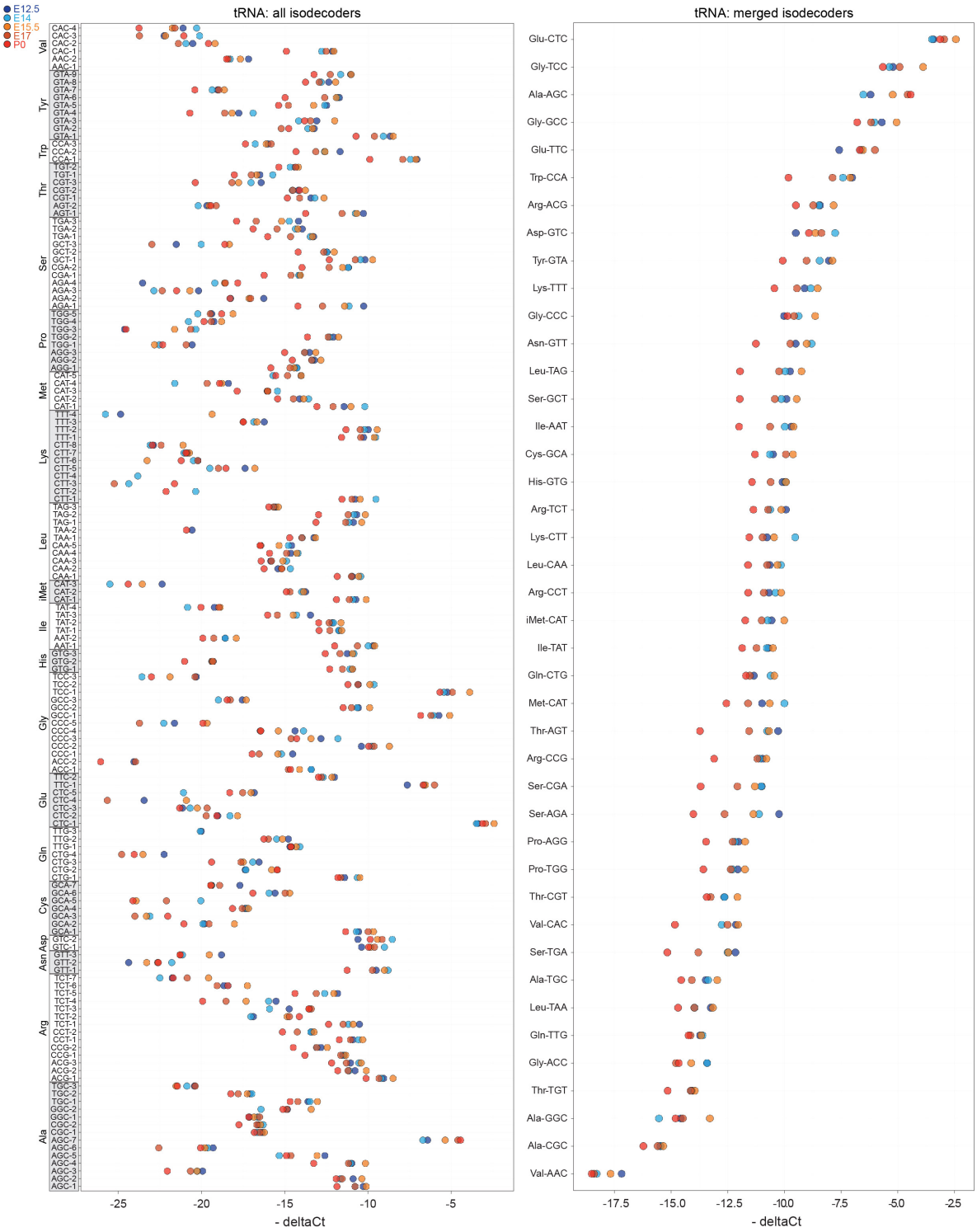

Extended Data Fig. 6. Neocortex tRNA qPCR array.
Total tRNA levels at each stage measured by qPCR array in biological duplicate, with Ct values for each tRNA isodecoder (left) or averaged across isodecoders (right) compared to the mean of 5S and 18S rRNA levels in each sample (delta Ct). Associated with **Fig. 5**. See also **Supplementary Table 4**.

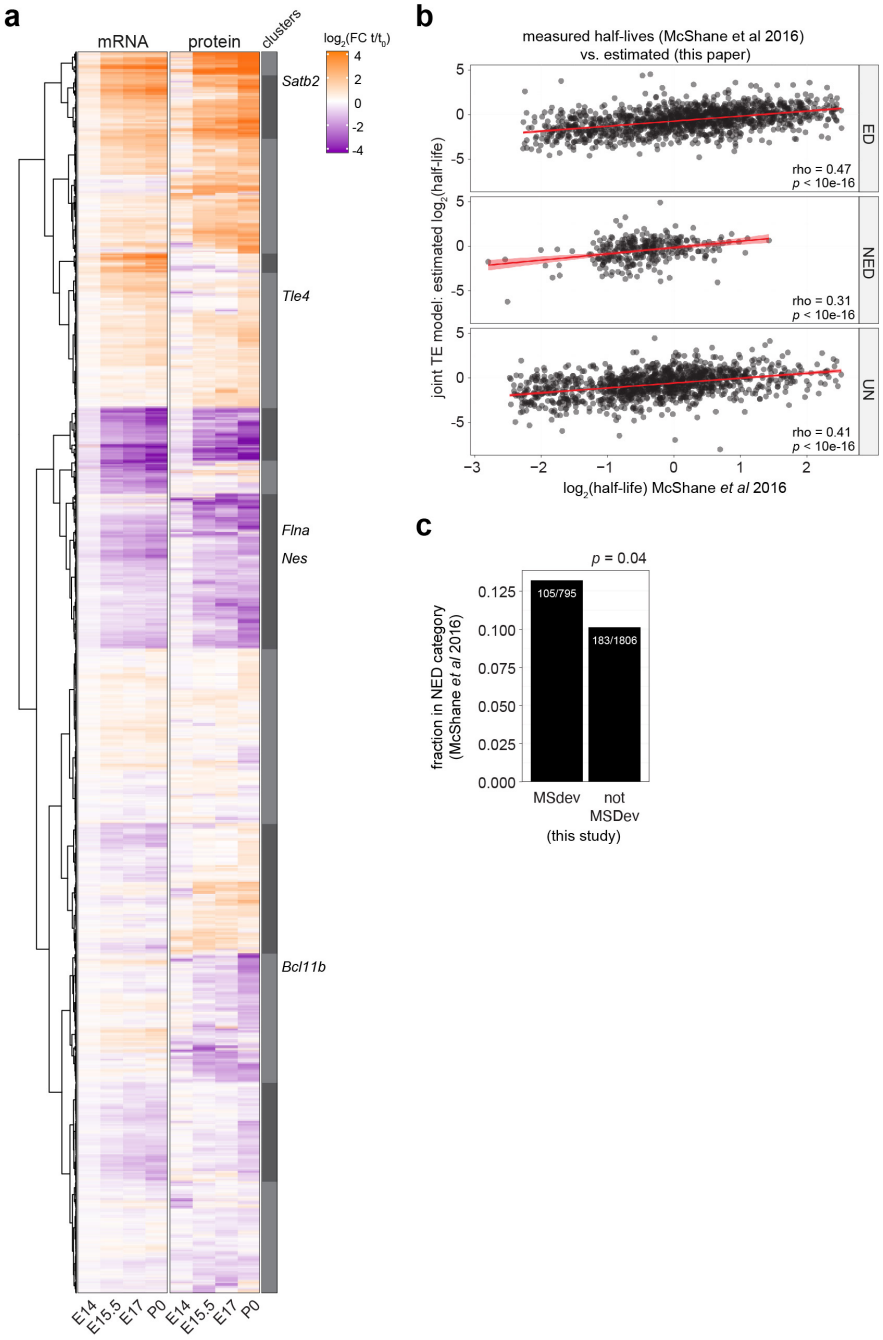

Extended Data Fig. 7. Modeling of mRNA translation.
a, Hierarchical clustering based on mRNA (RNA-seq) and protein (MS) expression trajectories per gene. Fold change expression increasing or decreasing from E12.5 (t_0) to subsequent developmental stages (t) shown in heat map. Neural stem cell and neuronal marker genes are indicated (right). **b**, Protein half-lives measured by SILAC MS and categorized as exponential decay (ED), non-exponential decay (NED), or neither (UN) in [47] correlated with the model estimates from our data as per [46]. **c**, The fraction of genes modeled as MS deviating or non-deviating in this study that are categorized as NED proteins in [47]. Associated with **Fig. 7**. See also **Supplementary Table 5**.

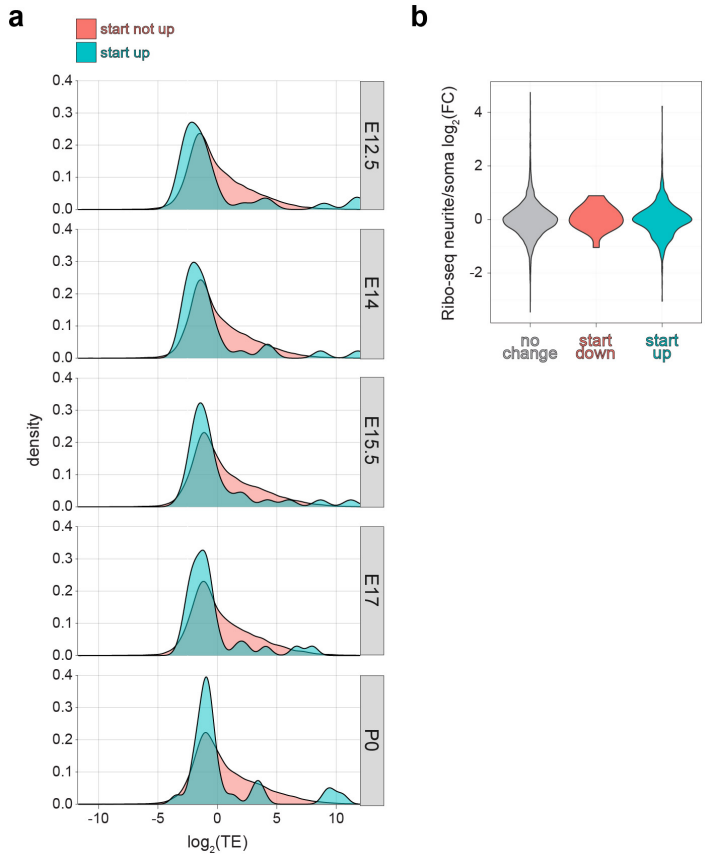

Extended Data Fig. 8. Start codon effect analysis.
a, TE distribution for genes with increasing start codon occupancy across developmental stages, compared to those without start occupancy changes. **b**, The association of mRNAs demonstrating start codon occupancy changes with translation in neurites vs. the soma of cultured neurons [81]. Associated with **Fig. 5**.